

NAD metabolic dependency in cancer is shaped by gene amplification and enhancer remodelling

Sudhir Chowdhry¹, Ciro Zanca^{1,8}, Utkrisht Rajkumar^{2,8}, Tomoyuki Koga¹, Yarui Diao^{3,4}, Ramya Raviram¹, Feng Liu⁵, Kristen Turner¹, Huijun Yang¹, Elizabeth Brunk¹, Junfeng Bi¹, Frank Furnari^{1,6}, Vineet Bafna², Bing Ren^{1,7} & Paul S. Mischel^{1,6*}

Precision oncology hinges on linking tumour genotype with molecularly targeted drugs¹; however, targeting the frequently dysregulated metabolic landscape of cancer has proven to be a major challenge². Here we show that tissue context is the major determinant of dependence on the nicotinamide adenine dinucleotide (NAD) metabolic pathway in cancer. By analysing more than 7,000 tumours and 2,600 matched normal samples of 19 tissue types, coupled with mathematical modelling and extensive in vitro and in vivo analyses, we identify a simple and actionable set of ‘rules’. If the rate-limiting enzyme of de novo NAD synthesis, NAPRT, is highly expressed in a normal tissue type, cancers that arise from that tissue will have a high frequency of NAPRT amplification and be completely and irreversibly dependent on NAPRT for survival. By contrast, tumours that arise from normal tissues that do not express NAPRT highly are entirely dependent on the NAD salvage pathway for survival. We identify the previously unknown enhancer that underlies this dependence. Amplification of NAPRT is shown to generate a pharmacologically actionable tumour cell dependence for survival. Dependence on another rate-limiting enzyme of the NAD synthesis pathway, NAMPT, as a result of enhancer remodelling is subject to resistance by NMRK1-dependent synthesis of NAD. These results identify a central role for tissue context in determining the choice of NAD biosynthetic pathway, explain the failure of NAMPT inhibitors, and pave the way for more effective treatments.

NAD is an essential small molecule co-factor in metabolic redox reactions^{3,4}, carrying high energy electrons to support oxidative phosphorylation by reversibly oxidizing or reducing NAD^{5–9}, and serving as a substrate for NAD-dependent enzymes that link cellular metabolism with epigenetic regulation and DNA damage repair^{3–6,10}. Mammalian cells make NAD by three different methods: (1) de novo synthesis from tryptophan; (2) generation from nicotinic acid using the Preiss–Handler (PH) pathway; or (3) synthesis from nicotinamide (NAM) or nicotinamide riboside via the salvage pathway^{3,4,8,11–14} (Fig. 1a, inset). The molecular mechanisms that dictate NAD synthesis pathway choice are not well understood.

Analysis of 63,865 samples from 216 cancer studies revealed that the rate-limiting enzymes of the PH, salvage and de novo NAD synthesis pathways—nicotinate phosphoribosyltransferase (NAPRT), nicotinamide phosphoribosyltransferase (NAMPT) and quinolinate phosphoribosyltransferase (QAPRT), respectively—were mutated in less than 1% of tumours. By contrast, the DNA copy numbers of NAPRT and NADSYN1 were increased in many cancer types, including prostate, ovarian and pancreatic cancers (Fig. 1a), and in 28 out of 54 cell lines profiled from the NCI-60 panel (Extended Data Fig. 1a, b) and 295 out of 947 (31%) CCLE cell lines (Extended Data Fig. 1c), significantly increasing gene expression (Extended Data Fig. 1c–e).

Amplification of PH-pathway genes (*NAPRT* and/or *NADSYN1*) in 7,328 tumours of various histological types was significantly

correlated with *NAPRT* gene expression in 2,644 matched normal tissues from which these tumours arose ($P < 0.0009$, Fig. 1b). Tissue-of-origin *NAPRT* gene expression was bimodally distributed ($P < 0.02$, Supplementary Table 1 and Methods), and 1,475 out of 1,573 *NAPRT*-amplified tumours (93%) arose from tissues that expressed high levels of the *NAPRT* transcript ($P < 0.0001$, Methods, Fig. 1b, Extended Data Fig. 1f–h), suggesting a role for tissue context in determining which cancers amplify *NAPRT*.

Non-cancerous cells were able to use any of the NAD biosynthetic pathways to maintain intracellular NAD levels and did not die in response to a specific NAMPT inhibitor, FK-866, or small interfering RNA (siRNA)-mediated genetic depletion of the rate-limiting enzymes of de novo NAD synthesis, or PH or salvage pathways (Extended Data Fig. 2a–g). By contrast, 29 out of 29 cancer cell lines with *NAPRT* amplification and/or *NADSYN1* amplification (PH-amplified), but 0 out of 25 non-PH-amplified cell lines (Extended Data Fig. 1a), depended on *NAPRT* and *NADSYN1* for survival (Fig. 1c, Extended Data Fig. 3a–c, Supplementary Table 2). Short hairpin RNAs (shRNAs) that target key enzymes of de novo NAD synthesis, or the PH and salvage pathways confirmed that PH-amplified cancer cells are entirely dependent on the PH pathway for maintenance of NAD and cell survival. By contrast, non-PH-amplified cancer cell lines depended exclusively on NAMPT and the salvage pathway (Fig. 1d, Extended Data Figs. 3d, 4a–c).

Detection of histone H3 lysine 27 acetylation (H3K27ac) using chromatin immunoprecipitation followed by sequencing (ChIP-seq)^{15,16} revealed a long-range, putative *NAMPT* enhancer 65 kb downstream of the *NAMPT* transcription start site on chromosome 7 (hg19: 105,856,018–105,860,658), specifically marked by H3K27ac and/or an accessible DNase I hypersensitive (DHS) signal in salvage-dependent, but not in PH-amplified cancer or normal cell lines (Fig. 2a). This 4.641-kb *cis*-regulatory region demonstrated potent enhancer activity when cloned either upstream or downstream of the 1.759-kb *NAMPT* promoter in reporter construct and tested in the salvage-dependent cancer cell lines, but not in PH-amplified or non-cancer control cell lines (Fig. 2b, Extended Data Fig. 5a). Fine-mapping of the 4.6-kb putative enhancer by stepwise 1-kb deletions or insertions identified the 1-kb enhancer ‘B’ region as responsible for *NAMPT* enhancer activity (Fig. 2c). CRISPR interference using catalytically inactive Cas9 (dCas9) fused to the Krüppel-associated box (KRAB) transcriptional repressor domain¹⁷ (Fig. 3a) confirmed that enhancer ‘B’: (1) controls expression of the *NAMPT* gene; (2) is the target of H3K27 acetylation; (3) regulates intracellular NAD levels; and (4) is required exclusively for tumour cell survival in an NAD-dependent manner in salvage-dependent cancer cells (Fig. 3b, c, Extended Data Fig. 5b, c).

We examined ChIP-seq data from the Encyclopedia of DNA Elements (ENCODE) project and performed a search for transcription factor motifs (Supplementary Table 3), focusing on five transcription factors—c-MYC, MAX, STAT3, FOXM1 and GATA3—that bind to

¹Ludwig Institute for Cancer Research, University of California at San Diego, La Jolla, CA, USA. ²Department of Computer Science and Engineering, University of California at San Diego, La Jolla, CA, USA. ³Department of Cell Biology, Regeneration Next Initiative, Duke University School of Medicine, Durham, NC, USA. ⁴Department of Orthopaedic Surgery, Regeneration Next Initiative, Duke University School of Medicine, Durham, NC, USA. ⁵National Research Center for Translational Medicine, Ruijin Hospital, Shanghai, China. ⁶Department of Pathology, University of California at San Diego, La Jolla, CA, USA. ⁷Department of Cellular and Molecular Medicine, Center for Epigenomics, and Moores Cancer Center, UC San Diego School of Medicine, La Jolla, CA, USA. ⁸These authors contributed equally: Ciro Zanca, Utkrisht Rajkumar. *e-mail: pmischel@ucsd.edu

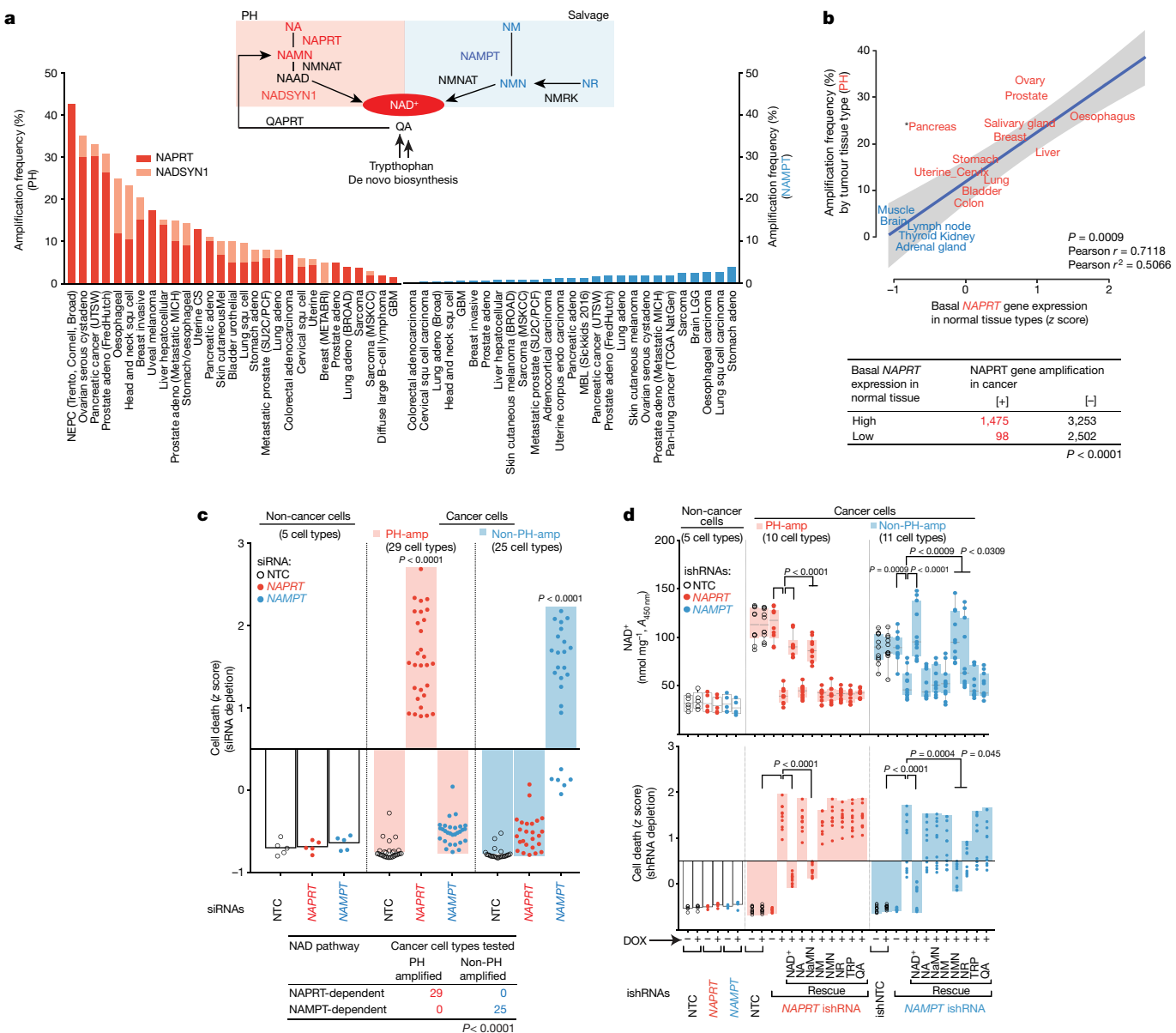


Fig. 1 | Tissue lineage-dependent, PH-pathway addiction in cancer driven by gene amplification. **a**, NAD⁺ biosynthesis pathways and gene amplification frequencies in cancer. adeno, adenocarcinoma; CS, carcinosarcoma; LGG, low grade glioma; MBL, monoclonal B-cell lymphocytosis; NA, nicotinic acid; NEPC, neuroendocrine prostate cancer; NM, nicotinamide; NR, nicotinamide riboside; NMNAT, nicotinamide mononucleotide adenyllyltransferase; QA, quinolinic acid; QAPRT, quinolinic acid phosphoribosyltransferase; squ, squamous. If the rate-limiting enzyme (NAPRT) of the de novo NAD biosynthesis PH pathway is highly expressed in a normal tissue type, cancers that arise from that tissue will have high amplification frequency of genes encoding key enzymes (such as NAPRT and NADSYN1) of the PH pathway. Analysis of more than 7,000 cancer samples of 23 histological types from The Cancer Genome Atlas (TCGA), and matched normal tissue samples from the Genotype-Tissue Expression (GTEx) and TCGA. To classify tissues as having ‘high’ or ‘low’ gene expression, the critical point of distribution was chosen at 10 reads per kilobase of transcript per million mapped

the NAMPT distal enhancer for further analysis (Fig. 3d, Extended Data Fig. 5d). siRNA-mediated knockdown demonstrated that c-MYC and MAX specifically regulate NAMPT enhancer activity in salvage-dependent cancer cells, as measured by H3K27ac chromatin immunoprecipitation combined with quantitative PCR (ChIP-qPCR) and a luciferase reporter assay (Fig. 3e, Extended Data Fig. 5e). These data identify a long-range NAMPT enhancer and reveal the epigenetic

reads (RPKM), at which the two distributions have identical density. **c**, Tissue context determines the dependence on the NAD metabolic pathway of cancer cells. Analysis of 54 tumour cell lines of 13 histological types from the NCI-60 panel, and 5 non-cancer cell lines. Cell death and sensitivity to knockdown were determined by propidium iodide staining (see Methods). NTC, non-targeting control. **d**, Unlike normal cells, PH-pathway-amplified tumour cells are completely dependent on NAPRT for survival. Tumour cells lacking these amplicons are entirely dependent on NAMPT for survival. The addition of indelible shRNAs (ishRNAs) that target key pathway intermediates confirms that survival dependence is completely mediated via NAD synthesis. Box plot with whiskers from minimum to maximum, and centre line at the median. Data in **c**, **d** represent independent biological replicates from three independent experiments. P values determined using Hartigan’s dip test followed by Bayesian probability statistics and two-sided Fisher’s exact test (**b**), or one-way analysis of variance (ANOVA) with Tukey’s multiple comparisons test (**c**, **d**).

mechanism that underlies the dependence of non-PH-amplified cancer cells on the NAD salvage pathway. Future studies are needed to identify further transcriptional regulators of this pathway.

We engineered NAPRT-amplified OV4 ovarian adenocarcinoma and non-PH-pathway-amplified H460 lung cancer cells to stably express doxycycline (DOX)-inducible shRNAs that target NAPRT, NADSYN1, NAMPT or NMRK1, and implanted the OV4 cells into the left flank,

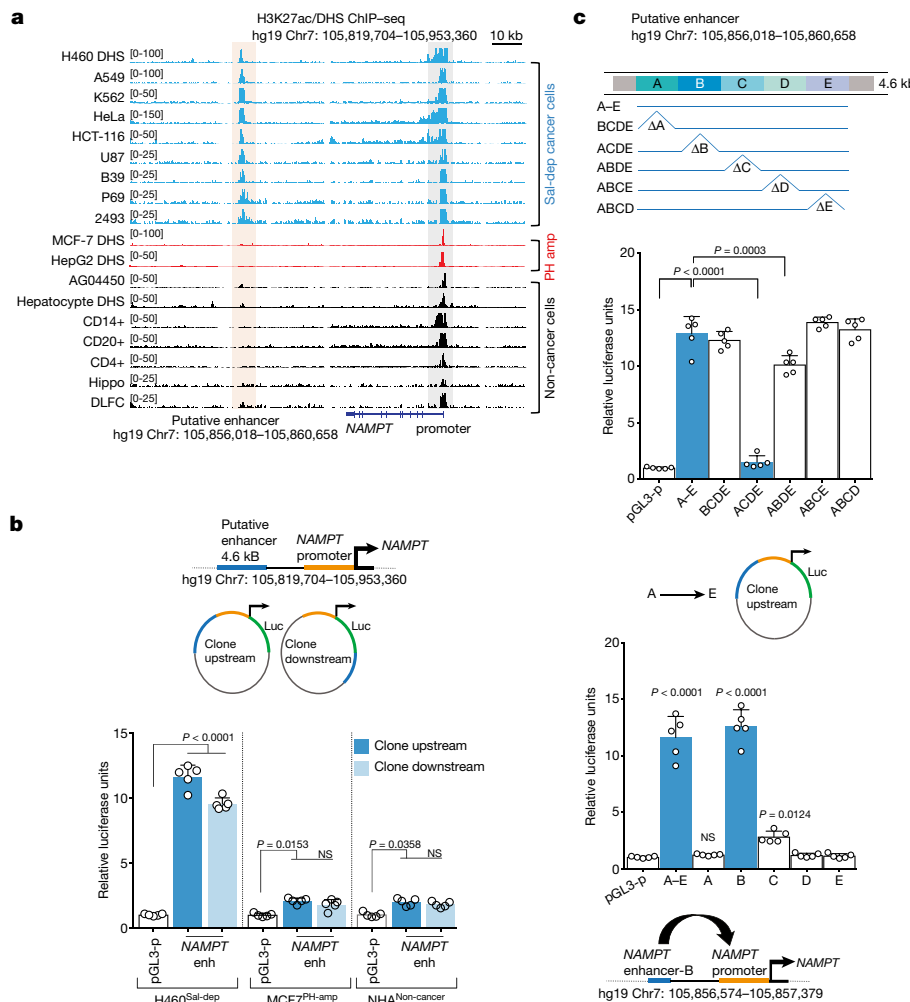


Fig. 2 | Identification of an epigenetic basis for NAMPT pathway addiction in non-PH-amplified cancers. **a**, Genome browser snapshot (top) illustrating H3K27ac and DHS ChIP-seq signal peaks across cancer cell lines and matched tumour tissue biopsies. Peach shaded region embedding H3K27ac or DHS peaks indicates a putative *NAMPT* enhancer, and the grey shaded region denotes the *NAMPT* promotor. **b**, Top, putative *NAMPT* enhancer locus cloned into an engineered luciferase reporter construct, upstream or downstream of the native *NAMPT* promoter. Bottom, bar plot shows luciferase reporter activity. **c**, Top, step-wise site-

and H460 cells into the right flank of nude mice. Intratumoral levels of NAD plummeted in OV4 tumours in response to DOX-induced expression of *NAPRT* or *NADSYN1* shRNA, causing tumours to completely and durably regress, and driving massive tumour cell death. Inducible depletion of *NAMPT* or *NMRK1* had no effect on intratumoral levels of NAD or on the growth of OV4 tumours in vivo (Fig. 4a, Extended Data Figs. 6a–d, i, 7a–d). Therefore, *NAPRT*-amplified tumours use the PH pathway exclusively for NAD homeostasis, and are entirely dependent on it for survival.

By contrast, H460 lung cancer cells were insensitive to depletion of *NAPRT*, but experienced a modest reduction in intratumoral levels of NAD that was associated with a small, but significant decrement in tumour proliferation and growth in response to induced *NAMPT* depletion (Fig. 4a, Extended Data Figs. 6a, e, f, i, 7a–d). In skeletal muscle cells, nicotinamide riboside has been shown to be an alternative source for *NAMPT*-independent synthesis of NAD via the salvage pathway using NMRK kinases¹⁸. Endogenous NMRK1 was sufficient to maintain NAD homeostasis and growth of tumour cell lines after inhibition of *NAMPT* (Extended Data Fig. 8a–e). Dual inhibition of both *NAMPT* and *NMRK1* caused intratumoral levels of NAD to decrease, resulting in complete and durable tumour regression and massive

directed mutagenesis to delete or clone small, approximately 1-kb-long individual enhancer fragments labelled A–E identifies the region required to drive *NAMPT* transcription in a luciferase reporter assay. Bottom, bar plots show luciferase reporter activity. Top plot, effect of deletion of enhancer fragments; bottom plot, effect of gain of enhancer fragments. Data in **b**, **c** are representative of five biological replicates from five independent experiments, and shown as mean \pm s.d. *P* values determined by one-way ANOVA with Tukey's multiple comparisons test. NS, not significant.

tumour cell death in vivo (Fig. 4b, Extended Data Figs. 6g, h, i, 7a–d), suggesting the need for combined inhibition of *NAMPT* and *NMRK* in non-PH-amplified tumours.

To determine whether biosynthetic NAD dependencies in cancer are pharmacologically actionable, we focused on a substrate competitive inhibitor of bacterial *NADSYN1*¹⁹, *N*-(3,4-dichlorophenyl)-4-{{[(4-nitrophenyl)carbamoyl]amino}benzenesulfonamide, hereafter referred to as *NADSYN1i*. There are, to our knowledge, no available crystal structures for the human *NADSYN1* enzyme, but several high-resolution structures are available for various bacterial species, such as *Bacillus subtilis* (Protein Data Bank (PDB) accession 1EE1)²⁰. Sequence alignments between the human and *B. subtilis* *NADSYN1* show limited overall conservation (23%), but a remarkably high degree of sequence conservation in the binding sites for nicotinic acid adenine dinucleotide (NAAD) and ATP²¹ (Fig. 4c). *NADSYN1i* has been suggested to bind competitively to the NAAD-binding site of *B. subtilis*^{19,22,23}, raising the possibility that *NADSYN1i* could also inhibit the human *NADSYN1* enzyme. *NADSYN1i* inhibited purified human *NADSYN1* enzyme activity in a dose-dependent manner (Fig. 4c) and potently and selectively inhibited the growth of PH-amplified cancer cell lines and reduced NAD levels, while having

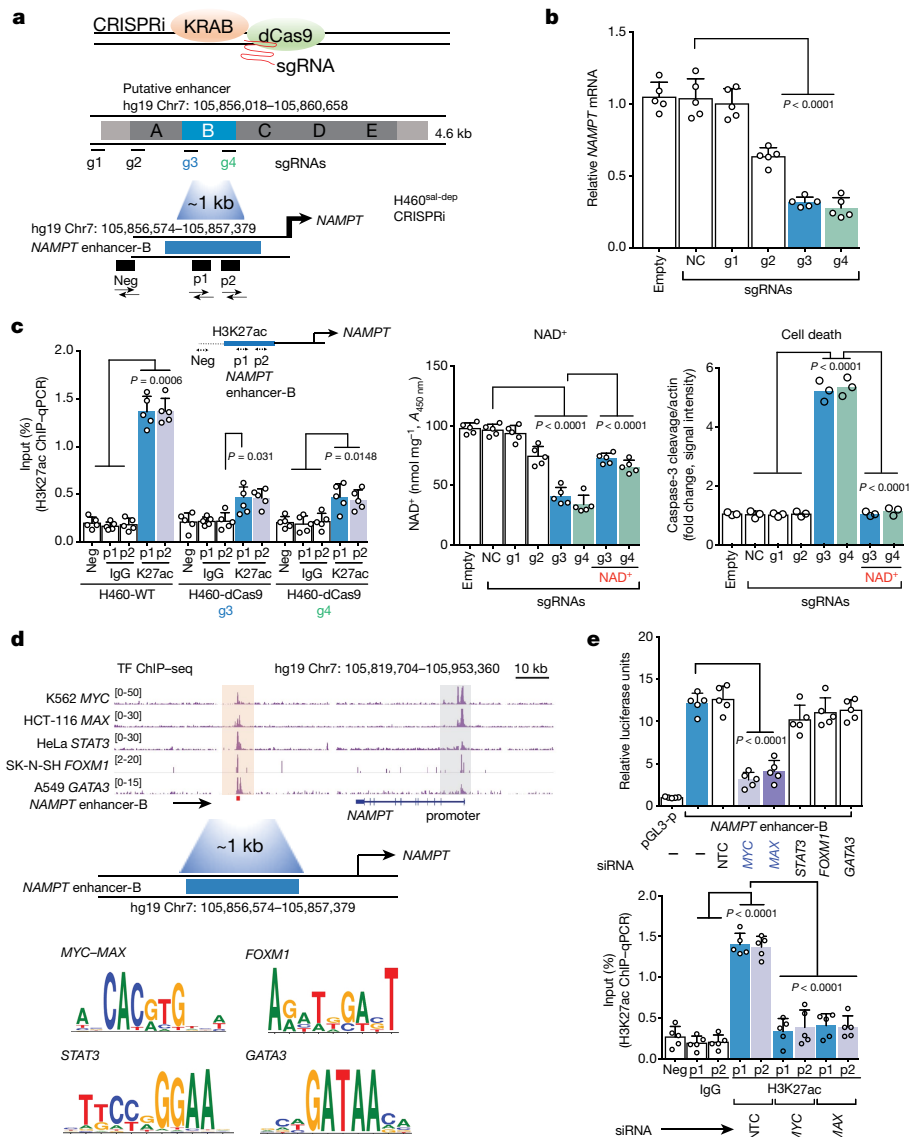


Fig. 3 | Dissection of the NAMPT enhancer and its regulation in cancer. **a**, Schematic overview of the CRISPR interference strategy used to identify the *cis*-regulatory element that controls NAMPT pathway addiction in cancer. Five different single-guide RNAs (sgRNAs) were individually fused to the dCas9-expressing construct. g1, sgRNA recognizing chromosome 7 genomic loci >20 kb away from the NAMPT ‘B’ enhancer region; g2, sgRNA recognizing 4.641-kb-long *cis*-regulatory region; g3 and g4, sgRNAs recognizing the NAMPT ‘B’ enhancer region. **b**, The specific enhancer elements that regulate NAMPT transcript levels. NC, non-coding sgRNA. **c**, H3K27ac ChIP-qPCR (left), NAD⁺ levels (middle) and cleaved

negligible effect on normal cells of non-PH-amplified cancer cell lines (Fig. 4c). NADSYN1i significantly inhibited the growth of NAPRT-amplified OV4 ovarian tumours and reduced intratumoral levels of NAD in mice in a dose-dependent manner, and had minimal effect on levels of NAD or tumour growth in salvage-dependent H460 lung tumours (Fig. 4d).

By contrast, the NAMPT inhibitor FK-866 selectively inhibited the growth of salvage-dependent cancer cell lines *in vitro* (Extended Data Fig. 9a–d), and inhibited the growth of H460 lung tumours in mice in a dose-dependent fashion, but had no effect on PH-amplified OV4 tumours *in vivo* (Fig. 4e, Extended Data Fig. 9e–h). Consistent with a central role for NMRK1 in bypassing NAMPT dependence, depletion of NMRK1 by shRNA knockdown significantly lowered the dose of FK-866 needed to inhibit growth of salvage-dependent non-PH-amplified tumours *in vitro* and *in vivo* (Fig. 4e, f, Extended Data Fig. 9d–h).

caspase-3 abundance (right). p1, primer pair 1; p2, primer pair 2; WT, wild type. **d**, Top, genome browser screenshot indicates transcription factor (TF) ChIP-seq signal across several cancer cell-types. Peach shaded region illustrate putative transcription factor recruitment sites that overlap with the NAMPT enhancer. Bottom, transcription factor motif analysis. **e**, Bar plots showing luciferase reporter assay (top) and H3K27ac ChIP-qPCR (bottom) to demonstrate MYC-MAX dependence of NAMPT enhancer activity. Data in **b**, **c**, **e** are representative of five biological replicates from five independent experiments, and shown as mean \pm s.d. P values determined by one-way ANOVA with Tukey’s multiple comparisons test.

Neither NAPRT nor NAMPT overexpression sensitized non-cancer cells (IMR90 and RPE-1) to NADSYN1i or FK-866 (Extended Data Fig. 10a–c). Furthermore, neither overexpression of NAMPT in OV4 cells nor overexpression of NAPRT in H460 cancer cells enabled tumour cells to switch their pathway dependence (Extended Data Fig. 10d–g). Therefore, further changes are likely to occur during tumorigenesis that contribute to NAD pathway addiction.

The complex interaction between local tissue contexts, lineage-dependent transcriptional repertoires, and altered tumour cell genotypes, and how this interaction affects which particular enzymes cancer cells depend on for survival is not well understood, raising a crucial challenge for translating biochemical and genetic insights about the metabolic landscape of cancer into more effective treatments for patients. The results presented here suggest that dependence on the NAD pathway in cancer arises from tissue-lineage-based gene

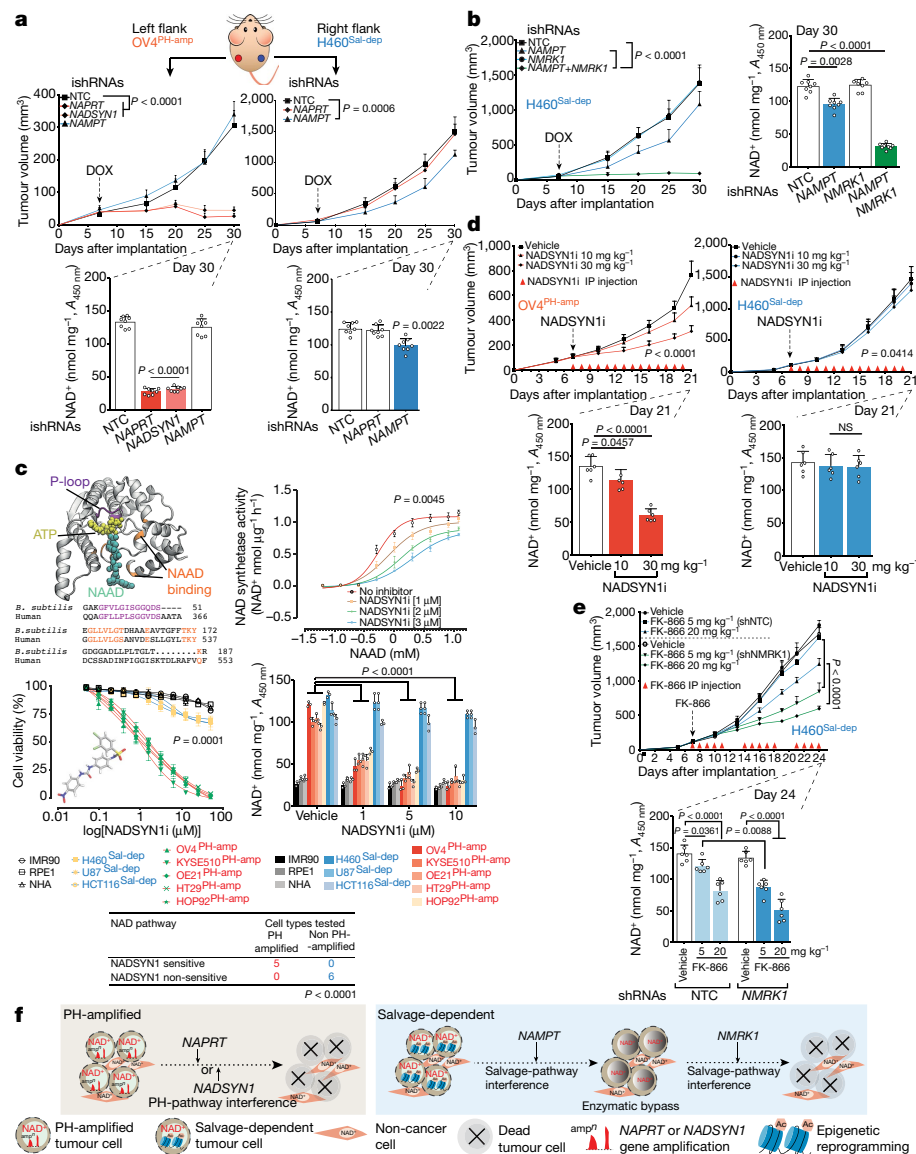


Fig. 4 | PH-pathway survival addiction is not subject to enzymatic bypass, resulting in massive tumour cell death in vivo, whereas epigenetically determined dependence on the salvage pathway is subject to resistance by enzymatic bypass. **a**, Top, tumour volumes of nude mice bearing engineered OV4^{PH-amp} and H460^{Sal-dep} cells implanted subcutaneously into the left or right flank. Bottom, intratumoral NAD⁺ levels. **b**, Left, tumour volume of nude mice bearing engineered H460^{Sal-dep} cells implanted subcutaneously. Right, intratumoral NAD⁺ levels. **c**, Crystal structure of glutamine-dependent NAD synthetase from *B. subtilis*, bound to ATP and NAAD. Sequence alignment of P loop (purple) and NAAD-binding sites (orange). NAD synthetase activity (top, right) of human recombinant enzyme. Cell viability (middle, left) of non-cancer and cancer cells treated with NADSYN1i for 72 h. Intracellular measurement of NAD⁺ levels (middle, right) in non-cancer and cancer cell lines ('PH-amp' and 'Sal-dep') treated with NADSYN1i. **d**, Top, tumour volumes of nude mice bearing OV4^{PH-amp} and H460^{Sal-dep} cells implanted subcutaneously into the left or right flank. Mice were injected

amplification and epigenetic remodelling, revealing genotype-selective, pharmacologically actionable dependencies that may potentially be used to develop more effective, precision treatments for cancer that target NAD metabolism.

Online content

Any methods, additional references, Nature Research reporting summaries, source data, statements of data availability and associated accession codes are available at <https://doi.org/10.1038/s41586-019-1150-2>.

intraperitoneally (IP) with NADSYN1i once daily. Bottom, intratumoral NAD⁺ levels. **e**, Top, tumour volume of nude mice bearing H460^{Sal-dep} cells implanted subcutaneously into the right flank. Mice were injected intraperitoneally with FK-866 twice daily. Bottom, intratumoral NAD⁺ levels. **f**, Schematic overview of the molecular basis of NAD metabolic pathway addiction in cancer. DOX treatment or drug administration was initiated on day 7 after implantation once the tumours were visible. Data are representative of eight (a, b, d, e: tumour volumes; a, b: NAD⁺ levels), six (d, e: NAD⁺ levels) and three (c) biological replicates. Data in a (top), b (left), d (top) and e (top) are mean tumour volume ± s.e.m. (n = 8 tumours per cohort from two independent experimental repeats). All bar plots and data in c (top right, middle left) are mean ± s.d. P values determined by two-sided Fisher's exact test (c), two-way ANOVA on repeated measurements over time (tumour volume data in a, b, d, e), or one-way ANOVA with Tukey's multiple comparisons test (bar plots in a–e, and non-linear curves in c).

Received: 13 July 2018; Accepted: 22 March 2019;

Published online: 24 April 2019

- Roychowdhury, S. & Chinnaiyan, A. M. Translating genomics for precision cancer medicine. *Annu. Rev. Genomics Hum. Genet.* **15**, 395–415 (2014).
- Mayers, J. R. & Vander Heiden, M. G. Nature and nurture: what determines tumor metabolic phenotypes? *Cancer Res.* **77**, 3131–3134 (2017).
- Cantó, C., Menzies, K. J. & Auwerx, J. NAD⁺ metabolism and the control of energy homeostasis: a balancing act between mitochondria and the nucleus. *Cell Metab.* **22**, 31–53 (2015).

4. Verdin, E. NAD⁺ in aging, metabolism, and neurodegeneration. *Science* **350**, 1208–1213 (2015).
5. Vander Heiden, M. G. & DeBerardinis, R. J. Understanding the intersections between metabolism and cancer biology. *Cell* **168**, 657–669 (2017).
6. Pavlova, N. N. & Thompson, C. B. The Emerging hallmarks of cancer metabolism. *Cell Metab.* **23**, 27–47 (2016).
7. Liu, L. et al. Quantitative analysis of NAD synthesis-breakdown fluxes. *Cell Metab.* **27**, 1067–1080 (2018).
8. Chiarugi, A., Dölle, C., Felici, R. & Ziegler, M. The NAD metabolome—a key determinant of cancer cell biology. *Nat. Rev. Cancer* **12**, 741–752 (2012).
9. Ryu, K. W. et al. Metabolic regulation of transcription through compartmentalized NAD⁺ biosynthesis. *Science* **360**, eaan5780 (2018).
10. Kaelin, W. G. Jr & McKnight, S. L. Influence of metabolism on epigenetics and disease. *Cell* **153**, 56–69 (2013).
11. Bogan, K. L. & Brenner, C. Nicotinic acid, nicotinamide, and nicotinamide riboside: a molecular evaluation of NAD⁺ precursor vitamins in human nutrition. *Annu. Rev. Nutr.* **28**, 115–130 (2008).
12. Katsuba, E. et al. De novo NAD⁺ synthesis enhances mitochondrial function and improves health. *Nature* **563**, 354–359 (2018).
13. Tateishi, K. et al. Extreme vulnerability of IDH1 mutant cancers to NAD⁺ depletion. *Cancer Cell* **28**, 773–784 (2015).
14. Piacente, F. et al. Nicotinic acid phosphoribosyltransferase regulates cancer cell metabolism, susceptibility to NAMPT inhibitors, and DNA repair. *Cancer Res.* **77**, 3857–3869 (2017).
15. Hnisz, D. et al. Super-enhancers in the control of cell identity and disease. *Cell* **155**, 934–947 (2013).
16. Leung, D. et al. Integrative analysis of haplotype-resolved epigenomes across human tissues. *Nature* **518**, 350–354 (2015).
17. Gilbert, L. A. et al. CRISPR-mediated modular RNA-guided regulation of transcription in eukaryotes. *Cell* **154**, 442–451 (2013).
18. Frederick, D. W. et al. Loss of NAD homeostasis leads to progressive and reversible degeneration of skeletal muscle. *Cell Metab.* **24**, 269–282 (2016).
19. Moro, W. B., Yang, Z., Kane, T. A., Brouillette, C. G. & Brouillette, W. J. Virtual screening to identify lead inhibitors for bacterial NAD synthetase (NADs). *Bioorg. Med. Chem. Lett.* **19**, 2001–2005 (2009).
20. Devedjiev, Y. et al. Stabilization of active-site loops in NH3-dependent NAD⁺ synthetase from *Bacillus subtilis*. *Acta Crystallogr. D* **57**, 806–812 (2001).
21. Hara, N. et al. Molecular identification of human glutamine- and ammonia-dependent NAD synthetases. Carbon-nitrogen hydrolase domain confers glutamine dependency. *J. Biol. Chem.* **278**, 10914–10921 (2003).
22. Velu, S. E., Luan, C. H., Delucas, L. J., Brouillette, C. G. & Brouillette, W. J. Tethered dimer inhibitors of NAD synthetase: parallel synthesis of an aryl-substituted SAR library. *J. Comb. Chem.* **7**, 898–904 (2005).
23. Wang, X. et al. Design, synthesis, and evaluation of substituted nicotinamide adenine dinucleotide (NAD⁺) synthetase inhibitors as potential antitubercular agents. *Bioorg. Med. Chem. Lett.* **27**, 4426–4430 (2017).

Acknowledgements We thank M. Meyerson for CRISPR interference plasmids; Mischel laboratory members and A. Shiao for suggestions; and A. Hwang for generating Extended Data Fig. 3a. This work was supported by Ludwig Institute for Cancer Research (P.S.M., B.R., F.F.), Defeat GBM program of the National Brain Tumor Society (P.S.M., F.F.), a Sharpe-National Brain Tumor Society Research Award (P.S.M.), NVIDIA Foundation, (P.S.M.), the Ben and Catherine Ivy foundation (P.S.M.), the Ziering Family Foundation in memory of Sig Ziering (P.S.M.) and NIH grants T32 CA009253 (R.R.), CA121938 (E.B.), NS73831 (P.S.M.), GM114362 (V.B.), NS80939 (F.F.), and NSF grants NSF-IIS-1318386 and NSF-DBI-1458557 (V.B.).

Author contributions S.C., V.B., B.R. and P.S.M. conceived and designed the study and interpreted results. S.C., V.B., B.R., F.F. and P.S.M. wrote the manuscript with critical suggestions from all authors. S.C., C.Z., T.K., H.Y., K.T., U.R., Y.D., R.R., F.L., E.B. and J.B. conducted all experiments. C.Z. and U.R. contributed equally.

Competing interests P.S.M. and V.B. are co-founders of Pretzel Therapeutics, Inc., have equity in the company and serve as consultants. B.R. is a co-founder of Arima Genomics, Inc., and has equity in the company.

Additional information

Extended data is available for this paper at <https://doi.org/10.1038/s41586-019-1150-2>.

Supplementary information is available for this paper at <https://doi.org/10.1038/s41586-019-1150-2>.

Reprints and permissions information is available at <http://www.nature.com/reprints>.

Correspondence and requests for materials should be addressed to P.S.M.

Publisher's note: Springer Nature remains neutral with regard to jurisdictional claims in published maps and institutional affiliations.

© The Author(s), under exclusive licence to Springer Nature Limited 2019

METHODS

Cell lines and cell culture. The NCI-60 cell-line panel (gift from A. Shiu, obtained from NCI) was grown in RPMI-1640 with 10% fetal bovine serum (FBS) under standard culture conditions. LNCaP, PC9, CAPAN1, U-87, HEK293, IMR90, HeLa, RPE-1 and MCF10A cells used in this study were obtained from ATCC and grown according to ATCC recommendations. Normal human astrocytes were obtained from Lonza and cultured according to Lonza-specific recommendations. GBM39 and GBM6 patient-derived neurosphere lines were cultured in NeuroCult medium supplemented with epidermal growth factor, fibroblast growth factor, and heparin. KYSE510, KYSE140 and BHY cells were obtained from Leibniz-Institut DSMZ-Deutsche Sammlung von Mikroorganismen und Zellkulturen GmbH, Germany, and OE21 cells were obtained from Sigma and maintained in RPMI-1640 with 10% FBS under standard culture conditions. Cell lines obtained from NCI, ATCC, DSMZ and Sigma were not authenticated. All cell lines were tested for mycoplasma contamination. All cells were cultured in a humidified incubator with 5% CO₂ at 37°C. Standard cell culture media formulations for both cancer and non-cancer models are supplemented with nicotinamide (4 mg ml⁻¹) and tryptophan (TRP, 16 mg ml⁻¹) but so far have not been shown to contain traces of nicotinic acid and nicotinamide riboside as NAD precursor. To address this issue, in our experimental cell culture model system, cells not only had constant access to nicotinamide and TRP, but also had access to the two missing precursors, nicotinic acid (4 mg ml⁻¹) and nicotinamide riboside (4 mg ml⁻¹).

Reagents and chemicals. Nicotinamide (N0636), nicotinic acid (N0761) and nicotinic acid mononucleotide (NAMN, N7764), TRP (T8941) were purchased from Sigma-Aldrich. Nicotinamide mononucleotide (NMN, 1094-61-7), quinolinic acid (89-00-9), nicotinamide riboside (1341-23-7) and FK-866 (658084-64-1) were purchased from Cayman chemicals, NADS1N1 was purchased from Vitas-M Laboratory (STK459768).

Plasmids. We developed a luciferase reporter system to assess genomic DNA fragments for promoter and enhancer activity. The *NAMPT* promoter when cloned upstream of the reporter gene should be able to activate luciferase reporter gene in a plasmid that does not already contain a promoter, whereas an enhancer is able to activate the luciferase reporter gene when cloned upstream or downstream of this reporter gene in a plasmid already containing an *NAMPT* promoter. The putative *NAMPT* enhancer (hg19_dna Chr7: 105,856,018–105,860,658) and the established *NAMPT* promoter (hg19_dna chr7:105,925,229–05,926,250) were PCR-amplified (Clontech, PrimeSTAR GXL DNA R050A) from human genomic DNA (bacterial artificial chromosomes, BACPAC Resources Center (BPRC), clone RP11-151E21, chromosome: chr7: 105,925,229–105,926,250). The pGL3 Basic (Promega, E1751) plasmid was digested with BglII/HindIII (New England Biolabs (NEB)) and the *NAMPT* promoter insert was ligated into a position upstream of the luciferase reporter gene generating pGL3-p reporter construct. To clone the putative *NAMPT* enhancer, pGL3-p promoter plasmid was digested with MluI/XHOI (NEB) and the putative *NAMPT* enhancer insert was ligated into a position upstream of the *NAMPT* promoter and luciferase reporter gene²⁴, generating the *NAMPT*-Enh reporter construct (clone upstream). To clone the putative *NAMPT* enhancer downstream of reporter gene, pGL3-p reporter construct was digested with XBAI and the putative *NAMPT* enhancer insert was ligated into a position downstream of the *NAMPT* promoter and luciferase gene²⁴, generating the *NAMPT*-Enh reporter construct (clone downstream). The internal region of the *NAMPT* enhancer is identical in both inserts, allowing cloning of a single PCR product into either construct. To dissect the *NAMPT* enhancer core, deletion mutants were generated using step-wise site-directed mutagenesis approach (Agilent, QuikChange II Site-Directed Mutagenesis 200523) to delete small ~1-kb enhancer fragments from the *NAMPT*-Enh reporter construct generating distinct *NAMPT*-Enh reporter constructs (BCDE; ACDE; ABDE; ABCE; ABCD). To individually clone small putative *NAMPT* enhancer fragments, the pGL3-p promoter plasmid was digested with MluI/Xhol and ~1-kb long *NAMPT* enhancer fragments inserts PCR-amplified from human genomic DNA were ligated into a position upstream of the *NAMPT* promoter and luciferase reporter gene, generating distinct *NAMPT*-Enh reporter constructs (A; B; C; D; and E). Stable cell lines overexpressing *NAMPT*, *NAPRT* or *NMRK1* were established using the lentiviral expression system. In brief, *nampt*-FLAG, *napt*-FLAG or *nmrk1*-FLAG plasmids were generated by cloning the respective cDNA into the p3xFLAG-tagged pLV cs2.0 lentiviral expression vector. The plasmid vector was digested using BAMHI and XMAI restriction sites. The PCR products were cloned into the digested plasmid using ligation independent cloning methodology using exonucleaseIII. Primers are listed in Supplementary Table 4.

Pan-cancer copy number alteration analysis. Pan-cancer copy number alteration data from 7,328 tumour-tissue samples of 23 histological types was obtained from The Cancer Genome Atlas (TCGA). Copy number alteration data for the entire cohort was downloaded and analysed using cBioPortal²⁵ (www.cbioportal.org). Copy number amplification datasets within the portal were generated by the GISTIC algorithm identifying significantly altered regions of amplification

or deletion across sets of patients. GISTIC-derived copy number analysis indicate copy-number level per gene, in which ‘−2’ is a deep loss (homozygous deletion), ‘−1’ is a shallow loss (heterozygous deletion), ‘0’ is diploid, ‘1’ indicates a low-level gain, and ‘2’ is a high-level amplification. mRNA data used for this analysis were RNA Seq V2 RSEM.

Estimation of lineage-specific amplification frequency model. Basal-normalized *NAPRT* transcript expression (RPKM, *z* score) from 19 normal tissues of origin (2,644 normal tissue samples) was obtained from GTEx²⁶ and TCGA²⁷ data to compute correlations between tissue-specific gene expression and tissue lineage-dependent PH-pathway gene amplification from matched 23 tumour types (7,328 tumour tissue samples). Processed RNA-seq files for each sample were downloaded from GDC (<https://portal.gdc.cancer.gov/repository>) and GTEx data portals (<https://gtexportal.org/home/datasets>). If the rate-limiting enzyme (*NAPRT*) of the de novo NAD biosynthesis PH pathway is highly expressed in a normal tissue type, cancers that arise from that tissue will have high amplification frequency of genes encoding key enzymes (*NAPRT*, NADS1N1) of the PH pathway. To compute tissue lineage-dependent association between genotype and *NAPRT* gene expression, Pearson correlation was tested between basal *NAPRT* transcript expression (RPKM) in the normal tissue of origin versus frequency of PH-pathway copy number amplification in the corresponding tumour tissue types. This statistically confirmed a strong correlation between normalized transcript expression of the *NAPRT* enzyme in a normal tissue of origin and the probability of copy number amplification of PH-pathway enzymes in corresponding tumour tissue type. To further compute the significance of this observation, we made three assertions. Specifically, if samples from a normal tissue of origin, *T*, have ‘high’ expression of the *NAPRT* gene, close to 50% of the tumour samples from *T* have PH-pathway copy number amplification. By contrast, if a normal tissue of origin, *T*, has ‘low’ expression, less than 10% of the tumour samples from *T* contain PH-pathway copy number amplification.

1. Basal-normalized *NAPRT* transcript expression (RPKM) in normal tissue of origin samples across all normal tissue types are bimodally distributed and can be treated as being sampled from one of two distributions (denoted as ‘high’ and ‘low’) (dip test of unimodality Extended Data Fig. 1g).

2. Basal-normalized *NAPRT* transcript expression in all samples from a tissue can be assigned to one of the two distributions but not both. Therefore, each tissue can be classified as having ‘high’ or ‘low’ expression of the gene.

3. Frequency of copy number amplification in a tissue is strongly associated with its classification as ‘high’ or ‘low’ (two-sided Fisher’s test, Fig. 1b).

For assertion 1, we computed the distribution on normalized *NAPRT* gene expression (RPKM). We combined all normalized *NAPRT* transcript expression data from 2,644 samples from 19 normal tissue of origin available from the TCGA and GTEx project and generated a frequency distribution. Using Hartigan’s dip test²⁸ with a null hypothesis of unimodality a *P* value of 0.0235899 was obtained, suggesting that we can reject the null hypothesis. We chose the critical point of the distribution as 10 RPKM. The critical point is defined as the point at which the two distributions have identical density. Given *NAPRT* gene expression *x* from a sample, let *P(x|C₁)* denote the probability that it is drawn from *C₁*. Assuming normality of the two distributions based on the law of large numbers, we computed the mean and standard deviation of each distribution to obtain *C₁(μ₁, σ₁)* and *C₂(μ₂, σ₂)*. For the 2,644 samples, we obtained (μ₁, σ₁) = (6.1935, 1.9625), and (μ₂, σ₂) = (30.906, 13.8312) and refer to *C₁* and *C₂* as ‘low’ and ‘high’, respectively.

We set,

$$P(x|C_1) \propto \frac{1}{\sqrt{2\pi\sigma_1^2}} \exp\left(-\frac{(x-\mu_1)^2}{\sigma_1^2}\right)$$

Tissue can be modelled of as a collection of independent sample *NAPRT* gene expression values, denoted by *T* = {x₁, x₂, ..., x_k}. The posterior probability of a distribution label *C* for tissue type *T* can be computed using the Bayesian formula,

$$\begin{aligned} P(C_1|T) &= \frac{P(T|C_1)P(C_1)}{P(T|C_1)P(C_1) + P(T|C_2)P(C_2)} \\ &= \frac{\prod_{x \in T} P(x|C_1)P(C_1)}{\prod_{x \in T} P(x|C_1)P(C_1) + \prod_{x \in T} P(x|C_2)P(C_2)} \end{aligned}$$

$$P(C_2|T) = 1 - P(C_1|T)$$

See Supplementary Table 1 for the posterior class probability of each tissue type. Supplementary Table 1 shows that we can assign a classification for each tissue type with high confidence. To validate the final assertion, we obtained 7,328 tumour samples from 23 tumour types and assigned to each sample a classification of ‘high’ or ‘low’, based on tissue type, as well as a binary classification of containing a copy number amplification or not. The 2 × 2 contingency table for the two-sided

Fisher's exact test in Fig. 1b partitions 7,328 tumour samples from 23 tumour types based on the amplification frequency of genes encoding key enzymes (NAPRT and NADSYN1) of the PH pathway and basal NAPRT transcript expression classification. We used the Fisher's exact test (Fig. 1b) to test for a null hypothesis of no association and obtained a *P* value of 1.7259×10^{-211} , suggesting that we can reject the null hypothesis.

Transient and stable knockdown of genes using siRNA, shRNA and ishRNA. Transient gene-silencing experiments were performed reverse transfecting siRNAs using Lipofectamine RNAiMAX Transfection Reagent (ThermoFisher Scientific) in growth media supplemented with 10% FBS. Growth media was replaced 24 h after transfection, and cells were collected 72 h after transfection. ON-TARGETplus SMART siRNA pools and their deconvoluted versions (Dharmacon), also including Silencer select siRNA's (Ambion-ThermoFisher Scientific) were used to target NAMPT, NMRK1, NMRK2, NAPRT and NADSYN1. Silencer Select Negative Control 2 siRNA (Ambion-ThermoFisher Scientific) that does not target any gene product was used as a negative targeting control. For generation of stable knockdown of cell lines lentiviral packaging/delivering system was performed. shRNA expressing pLKO.1 vector was introduced into cancer cell lines by lentiviral infection. Recombinant lentiviral particles were generated by transient transfection of HEK293T cells following a standard protocol. HEK293T cells were plated in a 100-mm dish and transfected (Xtremegene, Roche) with 6 µg of lentiviral DNA and lentiviral packaging system consisting of 0.6 µg of Rev, 0.6 µg of Gal/pol, 0.6 µg of TAT and 6 µg of VSVG. Viral supernatant was collected at 48 h and 72 h post transfection, centrifuged and filtered (0.45 µm) to remove any HEK293T cells. For transduction and stable knockdown of cell lines, lentiviral particles generated were added to cell culture medium containing 4 µg ml⁻¹ polybrene (Millipore). Forty-eight hours after infection, cells were selected using 1 mg ml⁻¹ puromycin for at least one week before being used for further experiments. For generation of stable inducible knockdown of cell lines lentiviral delivering system similar to the procedure described above was performed with the exception of using SMARTvector inducible system (Dharmacon) and also that cells were maintained in dialysed 10% FBS when generating lentiviral packaging/delivering system for transduction. For inducible RNAi experiments, stable knockdown of respective genes was induced using doxycycline at concentrations of 1.0–2.0 mg ml⁻¹. Sequence of siRNA, shRNA, ishRNA and relevant controls used in the study are listed in Supplementary Table 4.

Cell-death, apoptosis, viability and clonogenic assay. To examine cell death, cells were treated as indicated in the figure legends and stained with propidium iodide (Sigma-Aldrich). Adherent and floating cells were then analysed by flow cytometry using the BD LSRII flow cytometer (BD Biosciences). Data analysis was performed using FlowJo. For the siRNA screen, cells were seeded in duplicate for each condition in six-well culture plates at 100,000–200,000 cells per well. Cell death analyses were performed 72 h after transfection. For the shRNA screen, cells were seeded in duplicate for each condition in 60-mm dishes at 500,000 cells per dish. Cell death analyses were performed 7–10 days after infection/selection. For apoptosis assays, adherent and floating cells were lysed and homogenized with RIPA lysis buffer and immunoblotted for cleaved caspase-3 by western blotting. When measuring apoptosis after siRNA transfection, cells were obtained 72 h after transfection. For shRNA, cells were obtained 7–10 days after infection. To examine cell viability, cells were seeded in triplicate for each condition in six-well culture plates at 150,000–200,000 cells per well. Cell viability was analysed 72 h after siRNA transfection or FK-866 treatment²⁹. Total and live cells in each well were quantified by Trypan blue (Gibco) assay using a TC10 automatic cell counter (Bio-Rad). For clonogenic colony-formation assays, 300–500 cells were seeded in duplicate into six-well plates. Growth media was replaced every 2 days. At the indicated time point of around 2 weeks, remaining cells were fixed with 80% methanol and stained with crystal violet solution. Images were taken using digital imaging scanner (Bio-Rad). Colony formation was quantified by ImageJ software (NIH). **Immunoblotting and antibodies.** Cells were washed twice in ice-cold PBS, scraped and collected as pellets post centrifugation at 14,000 r.p.m. for 5 min. The pelleted cells were lysed with RIPA lysis buffer supplemented with protease inhibitor cocktail and phosphatase inhibitors. Lysates were collected and centrifuged at 14,000 r.p.m. for 10 min at 4 °C. Protein concentrations were determined by Bradford Assay using the Protein Assay Dye Reagent Concentrate. Equal amounts of protein extracts were separated and immunoblotted by SDS-PAGE 4–12% NuPAGE Bis-Tris Mini Gel (ThermoFisher Scientific). Proteins were later transferred using the Trans-Blot Turbo Transfer System (Bio-Rad) onto nitrocellulose membranes according to standard protocols. Membranes were blocked at room temperature with 5% bovine serum albumin in TBS with Tween buffer and incubated overnight with corresponding primary antibodies. Membranes were later incubated at room temperature with horseradish peroxidase-conjugated secondary antibodies. The immunoreactivity was detected with SuperSignal West Pico or Femto Chemiluminescent Substrate (ThermoFisher Scientific). The following antibodies were used: PBEF/NAMPT (Cell Signalling Technologies (CST), D1K6D

61122), NAPRT (ThermoFisher Scientific, PA5-31880), NAD synthetase (Abcam, ab171942), NMRK1 antibody (Santa Cruz, F-8 sc-398852), NMRK1 (Abcam, anti-C9orf95 antibody EPR11190 ab169548), NMRK2 or ITGB1BP3 (ThermoFisher Scientific, PA5-24607).

RNA extraction and quantitative PCR. Total RNA was extracted using RNeasy Mini Kit (QIAGEN). First-strand cDNA was synthesized using the SuperScript VILO cDNA synthesis kit (ThermoFisher Scientific). Quantitative PCR with reverse transcription (qRT-PCR) was performed using the iQ SYBR Green Supermix (Bio-Rad) on the CFX96 Touch Real Time PCR Detection system (Bio-Rad) following the manufacturer's instructions. Results were normalized to *TBP*, *B2M*, *YWHAZ* or *RPL13A* as the reference gene. Results were analysed using the ΔC_t . Primer sequences are listed in Supplementary Table 4.

DNA copy number. Copy number analyses of NAPRT, NADSYN1, NAMPT, NMRK1 and NMRK2 was quantified by qPCR, using the CFX96 Touch Real Time PCR Detection system (Bio-Rad). *RPPH1* and *HBB* were used as single copy reference control. PCR primer sequences for NAPRT, NADSYN1, NAMPT, NMRK1, NMRK2, *RPPH1* and *HBB* are listed in Supplementary Table 4. PCR primer (IDT) and the region of interest was selected by Primer Blast (<https://www.ncbi.nlm.nih.gov/tools/primer-blast/>) and USCS genome browser (<http://genome.ucsc.edu/cgi-bin/hgGateway>). Genomic DNA from 5 non-cancer and 54 cancer cell models was investigated. PCR reactions were carried in a final volume of 20 µl containing 20 ng genomic DNA (Qiagen), 300 nM primer and 1x SYBR green PCR Master Mix (Bio-Rad). PCR conditions are as follows: one cycle at 95 °C for 5 min, followed by 40 cycles each at 95 °C for 15 s and 60 °C for 1 min. Samples were analysed in triplicates. Each amplification reaction was checked for the absence of non-specific PCR products by melting curve analysis. Copy number analysis of NAPRT, NADSYN1, NAMPT, NMRK1 and NMRK2 was carried out using the comparative C_t method after validating that the efficiencies of PCR reactions of reference controls and genes under investigation are equal. Increase in gene copy number by 3–4 copies was defined as 'gain' while increase of ≥ 5 copies was categorized as 'amplification'. Primer sequences are listed in Supplementary Table 4.

Fluorescence in situ hybridization. Cells in log-growth phase were arrested in metaphase by the addition of KaryoMAX (Gibco) for 2 h. Cells were then collected and resuspended in a hypotonic solution (0.075 M KCl) for 15–30 min. Carnoy's fixative (3:1 methanol: glacial acetic acid) was added to stop the reaction. Double FISH was performed on the fixed metaphase spreads by adding the appropriate target DNA and centromere FISH probe. DNA was denatured at 75 °C for 3–5 min and the slides were allowed to hybridize overnight at 37 °C in a humidified chamber. Post overnight incubation slides were washed in pre-warmed 0.4 × SSC at 50 °C for 2 min, followed by a final wash in 2 × SSC 0.05% Tween-20. DAPI was used to counterstain metaphase cells and interphase nuclei and images were captured³⁰. FISH probes were purchased from Empire Genomics.

NAD measurement. Intracellular NAD pools were measured using NAD/NADH kit from Abcam (ab65348) according to the manufacturer's instructions.

NADSYN1 enzyme activity assay. NADSYN1 activity of the human recombinant protein is based on fluorometric measurements of NAD⁺ formed in the absence and presence of NADSYN1. Purified recombinant NADSYN1 (0.4 µg) was incubated with varied concentrations of NAAD⁺ (0–12 mM; 1 mM for a standard reaction) in the presence of saturating glutamine (20 mM) or 20 mM NH₄Cl as indicated in the reaction mixture (50 mM HEPES (pH 8.8), 2 mM ATP, 56 mM KCl, 5 mM MgCl₂, and 10 µg of bovine serum albumin. When glutamine was used as a substrate to measure NADSYN1 activity, 50 mM Tris-HCl (pH 7.5) was included instead of 50 mM HEPES (pH 8.8). The reaction mixture was incubated for 30 min at 37 °C. The enzyme reaction was terminated by adding 7 N NaOH and then incubated at 37 °C for 30 min to obtain the fluorescent product. Final product of the assay was measured by detecting Fluorescence using 380 nm for excitation and 460 nm for emission. Fluorescence intensity of NAD⁺ standards at known concentrations under similar reaction conditions was used to calculate the amount of NAD⁺. Specific NADSYN1 activity was determined by subtracting the NAD⁺ content of enzyme-deficient blanks from the NAD⁺ content of the complete reaction mixture^{21,31,32}.

Metabolic rescue experiments. For NAD⁺ rescue experiments, 200 µM of NAD⁺ (Sigma-Aldrich) was added to growth medium. For metabolic precursor rescue experiments, 500 µM of nicotinic acid, NAMN, nicotinamide, NMN, nicotinamide riboside, TRP or quinolinic acid was added independently to growth medium. Cells were treated with NAD⁺ or with individual precursors for the time periods as indicated in figure legends.

ChIP-seq analysis. ChIP-seq data for H3K27ac, DHS, and transcription factor ChIP-seq data for c-MYC, MAX, STAT3, FOXM1 and GATA3 are public datasets available from the ENCODE consortium, UCSC. We used the Fisher's exact test (Fig. 2a) to test the null hypothesis of no association and obtained a *P* value of 4.1×10^{-5} , suggesting that we can reject the null hypothesis. The putative enhancer was found specifically activated and accessible in 9 out of 9 salvage-dependent cancer models, but not (0 of 9) in the PH-amplified cancers or normal cell models.

CRISPR interference-mediated repression of the enhancer region. CRISPR inference dCas9 sgRNAs were identified using the MIT CRISPR Design tool, and control, non-targeting sgRNAs were selected from the GeCKOv2 library⁵⁴. All sgRNA sequences are listed in Supplementary Table 4. For repression of the NAMPT enhancer, lenti-KRAB-dCas9-blast was provided by M. Meyerson and X. Zhang³³. sgRNAs were cloned into lentiGuide-Puro using BsmBI as the restriction site (Addgene, 52963). Salvage dependent H460^{Sal-dep}, U87^{Sal-dep} and HCT116^{Sal-dep} cancer cells were first infected with lenti-KRAB-dCas9-blast and selected with 6 µg ml⁻¹ blasticidin. Cells stably expressing KRAB-dCas9 were then subsequently infected with sgRNAs and selected with 2 µg ml⁻¹ puromycin.

ChIP-qPCR. ChIP experiments were performed according to the manufacturer's instructions (CST, D1K6D 9004). In brief, around 1–2 × 10⁷ cells were crosslinked with 1% formaldehyde for 10 min at room temperature. Cells were washed twice in ice-cold PBS, scraped in ice-cold PBS with protease inhibitor cocktail and collected as pellets after centrifugation at 2,000g for 5 min at 4 °C. Nuclei pellet was incubated with micrococcal nuclease for 20 min at 37 °C with frequent mixing to digest DNA to length of approximately 150–900 bp. Samples were sonicated to break nuclear membrane and centrifuged at 9,400g for 10 min at 4 °C to clarify lysates. Chromatin samples were treated with RNaseA (5 µg ml⁻¹) and protease K (0.2 mg ml⁻¹) and purified using DNA purification spin columns. For chromatin immunoprecipitation 5–10 µg of digested, cross-linked chromatin per immunoprecipitation was used. Positive control histone H3 (CST, D2B12 4620) and negative control normal rabbit IgG (CST, 2729 samples) was included in all ChIP-qPCR experiments to test for the enrichment of RPL30 promotor. Sonicated chromatin samples were incubated with 5 µg H3K27ac antibody (active motif, 39133) or respective controls at 4 °C with rotation. After overnight incubation, protein G Magnetic beads were added to the ChIP reactions and incubated for additional 4 h at 4 °C with rotation to collect the immunoprecipitated chromatin. Magnetic beads were subsequently washed twice, each with 1 ml of low- to high-salt buffer. The chromatin was eluted in ChIP elution buffer upon incubation of magnetic beads at 65 °C for 30 min with gentle mixing. Input and chromatin samples were treated with 0.1 M NaCl, proteinase K (0.2 mg ml⁻¹), RNaseA (5 µg ml⁻¹) and reverse crosslinked at 65 °C overnight followed up with purification using DNA purification spin columns. qPCR was performed on the purified ChIP DNA using iQ SYBR Green Supermix (Bio-Rad) on the CFX96 Touch Real Time PCR Detection system (Bio-Rad) following the manufacturer's instructions. Enhancer occupancy was calculated as percentage of input DNA using the $\Delta\Delta C_t$ method. Primer sequences are listed in Supplementary Table 4.

Luciferase assay. Cells were transfected at 70% confluence using Lipofectamine2000 Reagent (ThermoFisher Scientific), according to the manufacturer's guidelines. In all transfections the pRL-TK Renilla reporter vector (Promega) was used as an internal control. Cells were lysed and *Renilla* and firefly luciferase activities were measured using the Dual-Luciferase Reporter Assay System (Promega) and a Tecan Infinite M1000 microplate reader. Luciferase activities were normalized to *Renilla* internal control luminescence.

Xenografts. All procedures were reviewed and approved by the Institutional Animal Use and Care Committee (IACUC) at University of California, San Diego. Tumour size must not exceed 20 mm at the largest diameter and this tumour threshold was never exceeded in any experiment. Five-six-week-old female athymic nu/nu mice were purchased from Harlan Sprague Dawley. Subcutaneous tumours were established by injection of 5 × 10⁵ parental or genetically engineered lung cancer H460 cells, and 3 × 10⁶ parental and 2.5 × 10⁶ genetically engineered OV4 cells, implanted subcutaneously into the flanks of immune-compromised female mice. Genetically engineered OV4^{PH-amp} cells stably expressing DOX-inducible shRNA against *NAPRT* (ishNAPRT), *NADSYN1* (ishNADSYN1), *NAMPT* (ishNAMPT) or *NMRK1* (ishNMRK1) were independently inoculated at the left flank, and H460^{Sal-dep} cells stably expressing DOX-inducible shRNA against *NAPRT* (ishNAPRT), *NAMPT* (ishNAMPT), *NMRK1* (ishNMRK1) or both *NAMPT* and *NMRK1* (ishNAMPT + ishNMRK1) were independently inoculated at the right flank in individual mice. To test for the rescue of the knock-down phenotype, OV4^{PH-amp} or H460^{Sal-dep} cells stably expressing DOX-inducible shRNA targeting the 3' UTR of the target genes, *NAPRT* (ishNAPRT), *NAMPT* (ishNAMPT) or *NMRK1* (ishNMRK1) or co-deletion of *NAMPT* and *NMRK1* (ishNAMPT+NMRK1) were subcutaneously implanted at the left flank in individual mice. The same clone of stably engineered OV4^{PH-amp} or H460^{Sal-dep} cells but with expression of exogenous cDNA corresponding to the target not susceptible to silencing compared to the endogenous copy, (ishNAPRT(+naprt-Flag)), (ishNAMPT(+nampt-Flag)) or (ishNAMPT+NMRK1(+nmrk1-Flag)) were subcutaneously implanted at the right flank in individual mice. ishNTC was used as a non-targeting control inducible shRNA for both tumour types. Each cohort categorized for both tumour types consisted of eight mice. After implantation of tumour cells, mice were randomized and then allocated into cages. Mice were fed DOX-containing chow (200 mg kg⁻¹, Bio-Serv), starting 7 days after implantation until the end of the experiment. For FK-866 treatment, tumour-bearing

mice were intraperitoneally injected with FK-866 at 5 mg kg⁻¹ or 20 mg kg⁻¹ or with PBS twice daily for 5 days per week for 3 weeks. For NADSYN1i treatment, tumour-bearing mice were intraperitoneally injected with NADSYN1i at 10 mg kg⁻¹ or 30 mg kg⁻¹ or with PBS once daily for 2 weeks. Tumour volume was monitored every 3–5 days over a 30-day period using electronic calipers. Tumour volumes were calculated by caliper measurements of the short (*a*) and long (*b*) tumour diameters (volume = $a^2 \times b/2$) or of tumour height (*h*), short (*a*) and long (*b*) tumour width (volume = $h \times a \times b/2$) depending on tumour shape (mean tumour volume ± s.e.m.). In vivo tumour models do not mimic human physiology considering the bioavailability of NAD precursors. In the mouse DOX diet, only niacin (86.9 mg kg⁻¹) and TRP (2.5 g kg⁻¹) are present, and the availability of nicotinic acid and nicotinamide riboside is unique and only orally bioavailable. Therefore, to mimic human physiology and pathophysiology where there is a ubiquitous presence of all the NAD precursors, nicotinamide, nicotinamide riboside, nicotinic acid and TRP were orally provided in the drinking water ad libitum (200 mg kg⁻¹ day⁻¹) to nude mice bearing tumours.

Immunohistochemistry and tissue Ki67 staining. Formalin-fixed, paraffin-embedded (FFPE) tissue sections were prepared by the Histology Core Facility at UCSD Moores Cancer Center. Immunohistochemistry was performed according to standard procedures. Antigen was retrieved by boiling slides in 0.01 M of sodium citrate (pH 6.0) in a microwave for 15 min. Sections were incubated with primary Ki67 antibody (ThermoFisher Scientific, PA5-16785) at 4 °C overnight, followed by incubation with biotinylated secondary antibodies at room temperature for 30 min. Three representative images from each immunostained section were captured using DP 25 camera mounted on an Olympus BX43 microscope at 40× magnification. Quantitative analysis of the IHC images was performed using image analysing software (Visiopharm).

Tissue TUNEL staining. Cell death analysis was conducted in xenografts using the *In situ* Cell Death Detection kit, Fluorescein (Sigma-Aldrich) according to the manufacturer's protocol. In brief, paraffin embedded tissues were deparaffinized with xylene and rehydrated with ethanol, followed by treatment with proteinase K (5 µg ml⁻¹, New England Biolabs). Sections were then incubated with reaction buffer for 1 h at 37 °C in a humidified chamber with no access to light. DAPI was used to stain DNA. Images were acquired with an Olympus IX81 microscope. Three representative images from each section were captured using DP 25 camera mounted on an Olympus BX43 microscope at 40× magnification. Quantitative analysis of the images detecting TUNEL⁺ nuclei was performed using ImageJ software (NIH).

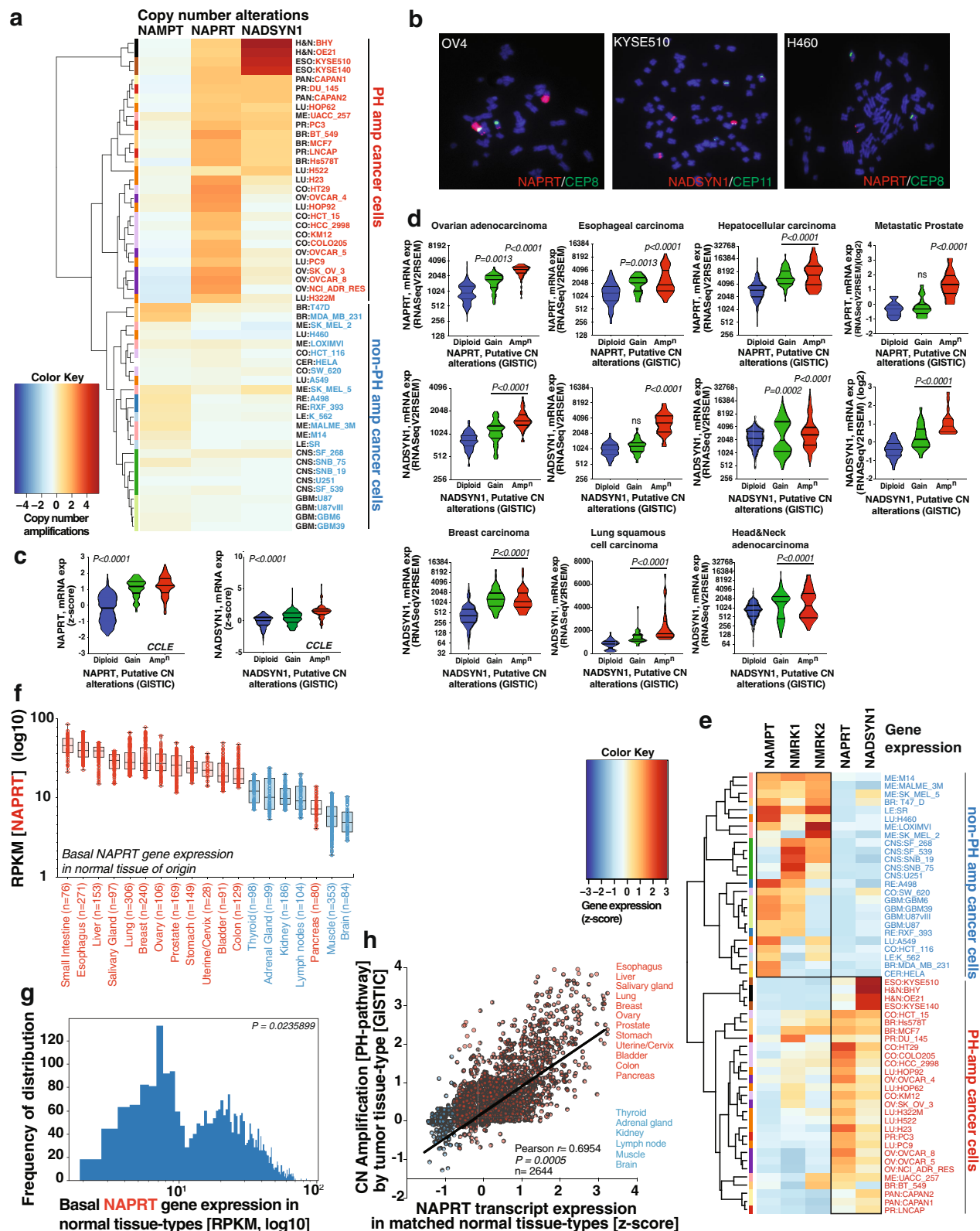
Statistics and reproducibility. Graphpad Prism software was used to conduct the statistical analysis of all data. No statistical methods were used to predetermine sample size. For xenograft experiments, female athymic nu/nu mice injected with tumour cells were randomized before being allocated to respective cages. All other experiments conducted for the study were not randomized, and the investigators were not blinded to either allocation during experiments or to outcome assessments. Experiments in Fig. 1a, b, 2a, 3d, 4c (structural analysis), Extended Data Figs. 1c, d, f-h, 5d were performed once; experiments in Fig. 4a–e, Extended Data Figs. 1a, b, e, 4a, c, 5c, 6a–i, 7a–d, 8a (crystal violet staining), 8b, 9c, e–h, 10a, d, e were performed twice with similar observations. All other experiments were performed at least three times with similar observations. Variation in data in all experiments is presented as mean ± s.d. except for variation for xenograft tumour volume, which is illustrated as the s.e.m. In Extended Data Fig. 1c, d, quantitative results were assessed by unpaired Student's *t*-test after confirming that the data met appropriate assumptions. The Student's *t*-test assumed two-tailed distributions to calculate statistical significance between groups. For comparisons among three or more groups, statistical significance was assessed using one-way ANOVA followed by Tukey's multiple comparisons test. To examine significance in xenograft tumour growth between two or among three or more groups, statistical significance was assessed using two-way ANOVA, to calculate significance on repeated measurements over time followed by Tukey's multiple comparisons test. As required for ANOVA, we first tested, if there was homogeneity of variation among the groups using the Brown-Forsythe test. In all xenograft assays, subcutaneous tumours were established in 5–6-week-old female athymic nu/nu mice and randomized into different cohorts. Each categorized cohort for both tumour-types consisted of eight mice.

Reporting summary. Further information on research design is available in the Nature Research Reporting Summary linked to this paper.

Data availability

The data supporting the findings of this study are available within the paper and its Supplementary Information. Source Data for all figures are available online. Data are available from the corresponding author upon reasonable request.

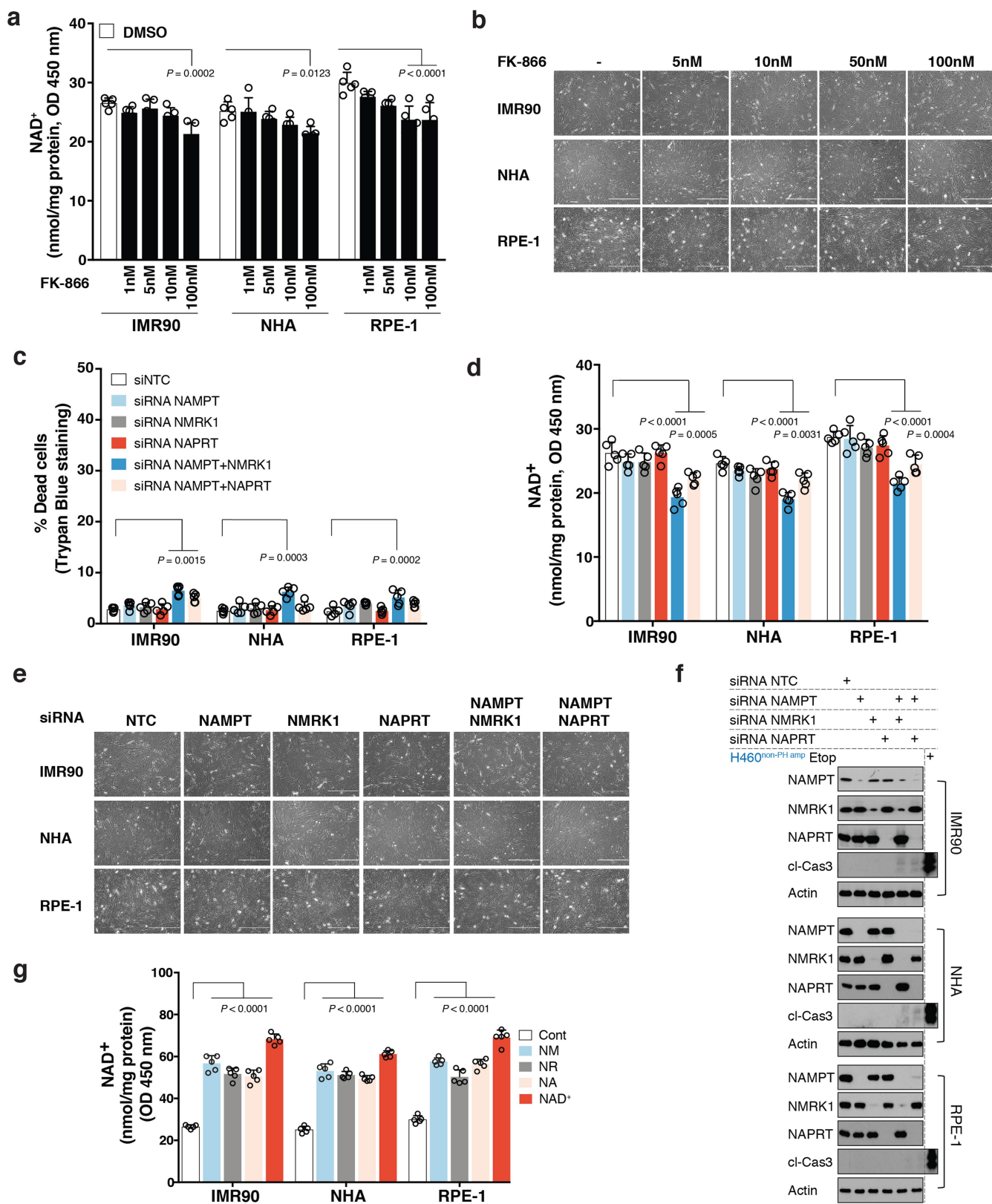
25. Cerami, E. et al. The cBio cancer genomics portal: an open platform for exploring multidimensional cancer genomics data. *Cancer Discov.* **2**, 401–404 (2012).
26. Lonsdale, J. et al. The Genotype-Tissue Expression (GTEx) project. *Nat. Genetics* **45**, 580–585 (2013).
27. Grossman, R. L. et al. Toward a shared vision for cancer genomic data. *N. Engl. J. Med.* **375**, 1109–1112 (2016).
28. Hartigan, J. A. & Hartigan, P. M. The dip test of unimodality. *Ann. Stat.* **13**, 70–84 (1985).
29. Hasmann, M. & Schemainda, I. FK866, a highly specific noncompetitive inhibitor of nicotinamide phosphoribosyltransferase, represents a novel mechanism for induction of tumor cell apoptosis. *Cancer Res.* **63**, 7436–7442 (2003).
30. Turner, K. M. et al. Extrachromosomal oncogene amplification drives tumour evolution and genetic heterogeneity. *Nature* **543**, 122–125 (2017).
31. Wojcik, M., Seidle, H. F., Bieganowski, P. & Brenner, C. Glutamine-dependent NAD⁺ synthetase. How a two-domain, three-substrate enzyme avoids waste. *J. Biol. Chem.* **281**, 33395–33402 (2006).
32. Zalkin, H. NAD synthetase. *Methods Enzymol.* **113**, 297–302 (1985).
33. Zhang, X. et al. Identification of focally amplified lineage-specific super-enhancers in human epithelial cancers. *Nat. Genet.* **48**, 176–182 (2016).



Extended Data Fig. 1 | See next page for caption.

Extended Data Fig. 1 | Tissue lineage-dependent, PH-pathway gene amplification in cancer. **a**, Heatmap illustrating copy number (CN) alterations (z score) for *NAMPT*, *NAPRT* and *NADSYN1* across cancer cell types ($n = 54$ cell types). **b**, Representative FISH images of cells in metaphase from two independent experiments with similar observations displaying *NAPRT* and *NADSYN1* gene amplification on homogenously staining regions in PH-amplified (OV4^{PH-amp} and KYSE510^{PH-amp}) and non-PH-amplified (H460^{non-PH-amp}) cancer cell lines as indicated. **c**, Violin plots of *NAPRT* (left) or *NADSYN1* (right) mRNA expression against putative copy number alterations from several tumour types from CCLE ($n = 947$ from biologically independent samples including shallow/deep deletion). **d**, Violin plots of *NAPRT* or *NADSYN1* mRNA expression stratified by *NAPRT* and *NADSYN1* copy number alterations in multiple tumour types from cBioportal (ovarian adenocarcinoma: $n = 403$; oesophageal carcinoma: $n = 150$; hepatocellular carcinoma: $n = 341$; metastatic prostate adenocarcinoma: $n = 99$; breast carcinoma: $n = 311$; lung squamous cell carcinoma: $n = 163$; head and neck adenocarcinoma: $n = 503$, from biologically independent samples). Violin plots display median, first and third quartiles. **e**, Heatmap illustrating differential gene expression profiles of NAD biosynthesis

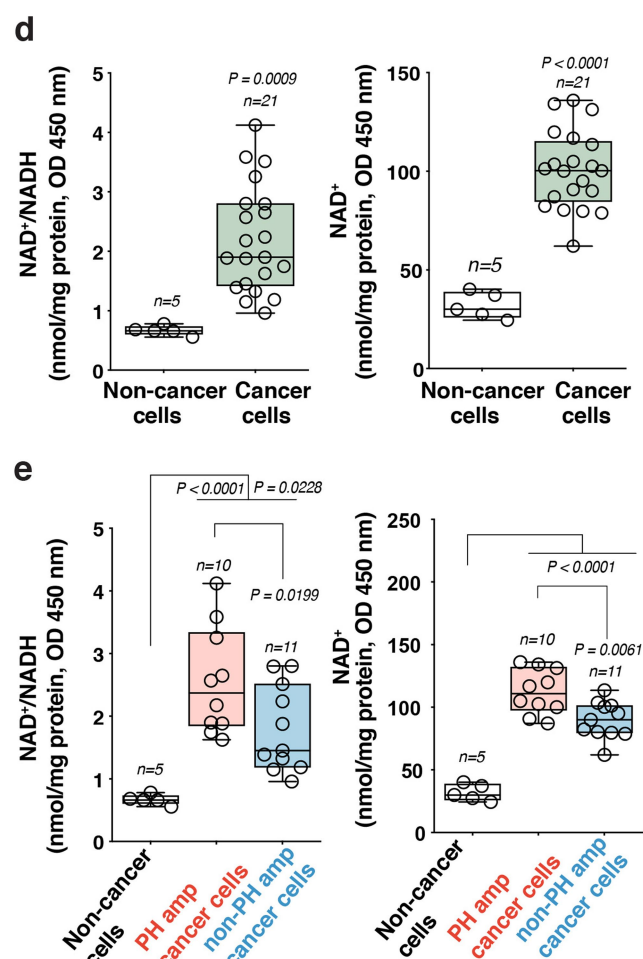
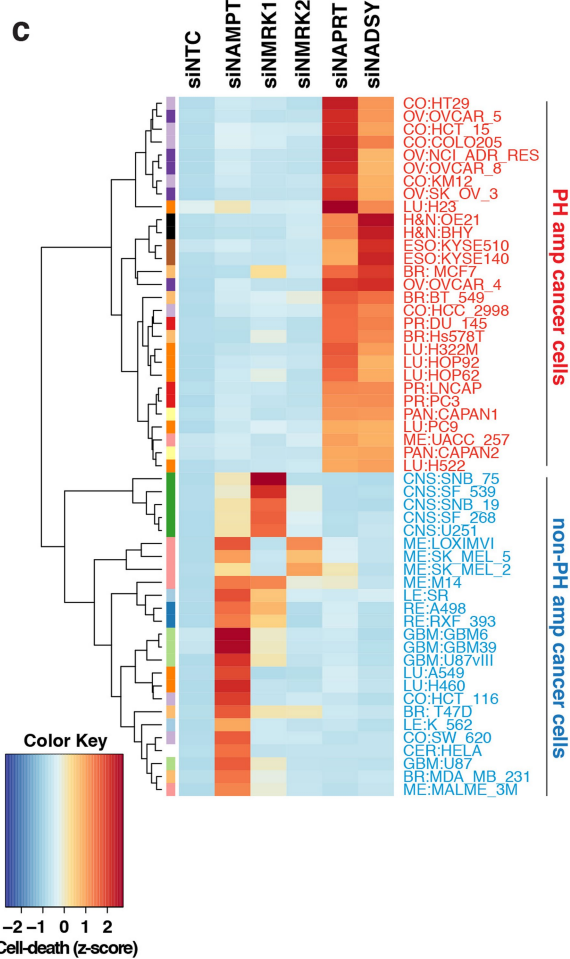
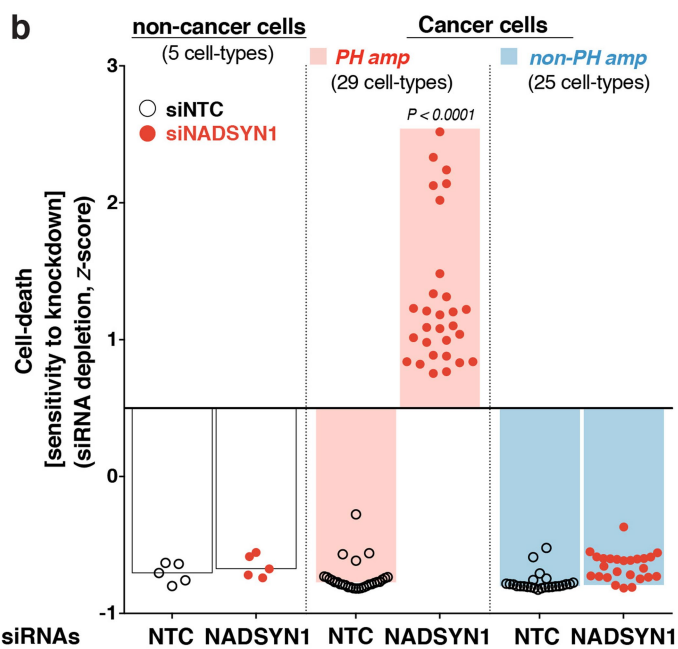
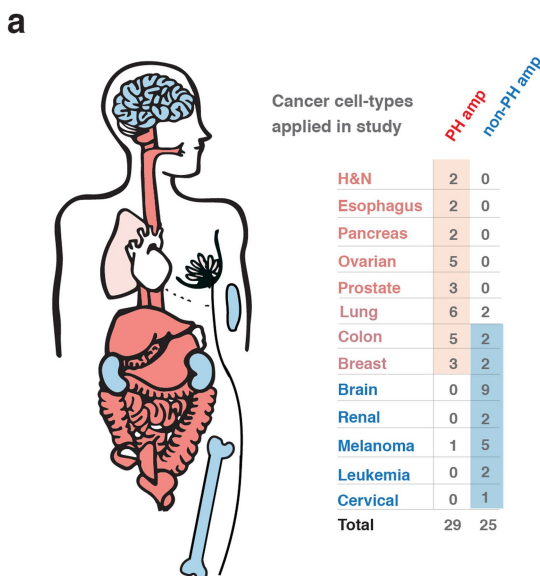
enzymes in PH-amplified and non-PH-amplified cancer cell types (z score, $n = 54$). Cancer cell lines amplified for the PH-pathway enzymes (*NAPRT* or *NADSYN1*) are denoted as ‘PH-amp’ in red, and cancer cell lines that are not amplified for *NAPRT* or *NADSYN1* are denoted as ‘non-PH-amp’ in blue. **f**, Box and whisker plots showing normalized *NAPRT* transcript level (RPKM) in 19 distinct normal tissue of origin obtained from the GTEx and TCGA portal (www.gtexportal.org; www.portal.gdc.cancer.gov/repository). Box plot as in Fig. 1d, with all points are plotted according to the Tukey method. **g**, Bimodal distribution based on dip test of unimodality of two distributions stratified as ‘high’ and ‘low’ ($n = 2,644$ biologically independent samples). To classify tissues as having ‘high’ or ‘low’ gene expression, the critical point of distribution was chosen at 10 RPKM, at which the two distributions have identical density. **h**, Pearson correlation between expression of the *NAPRT* transcript (RPKM, z score) in 19 normal tissues and *NAPRT* or *NADSYN1* copy number in 23 cancer types ($n = 2,644$ biologically independent samples). Statistical significance for mRNA expression against putative copy number alterations was assessed using two-tailed unpaired Student’s *t*-test (**c**, **d**). Experiments in **a** and **e** were repeated twice.



Extended Data Fig. 2 | See next page for caption.

Extended Data Fig. 2 | Non-cancer cells are not dependent on a single NAD biosynthetic pathway for survival. **a**, Intracellular measurement of NAD⁺ levels in non-cancer cells after treatment with increasing doses of the NAMPT inhibitor FK-866 for 72 h. **b**, Representative images of non-cancer cells from one of two independent experiments, treated with increasing doses of FK-866 for 72 h. Both biological replicates showed similar results. Original magnification, $\times 10$. **c–f**, Non-cancer cells transfected with siRNAs targeting *NAMPT* (siNAMPT), *NMRK1* (siNMRK1) and *NAPRT* (siNAPRT), either individually or in combination. A non-targeting control siRNA (siNTC) was used as a negative control. **c**, Scattered data plots with bars representing percentage of cell death as assessed by trypan blue exclusion assay in non-cancer cells. **d**, Intracellular measurement of NAD⁺ levels in non-cancer cells. **e**, Representative images of non-cancer cells from one of two independent experiments, transfected with siRNAs targeting *NAMPT*, *NMRK1* and

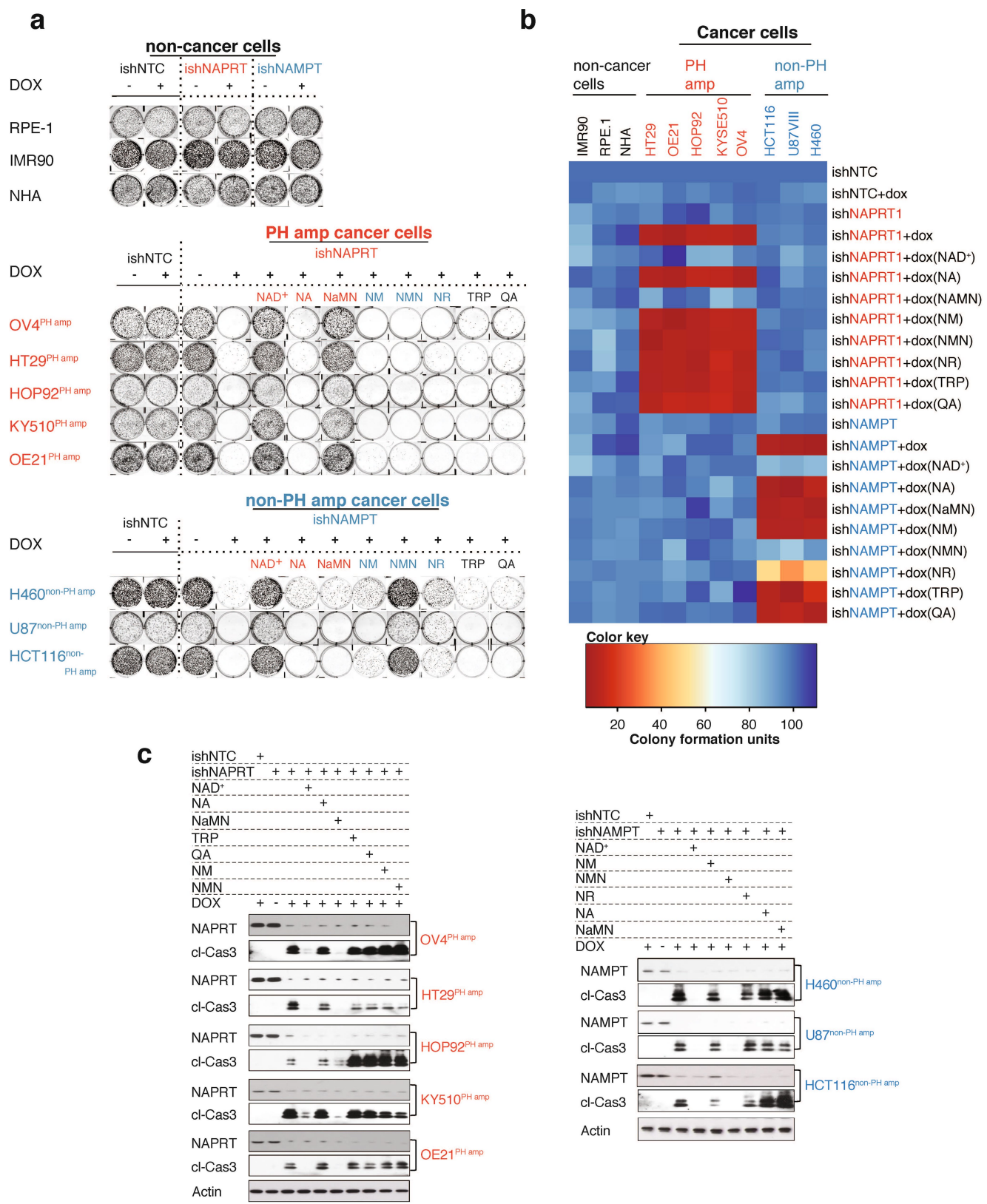
NAPRT, either individually or in combination. Both biological replicates showed similar results. Original magnification, $\times 10$. **f**, Immunoblotting for cleaved caspase-3 (Cl-cas3) as a measure of cell death and to test for abundance of NAMPT, NMRK1 and NAPRT protein expression. Protein lysates from H460 cancer cells treated with etoposide (Etop) were used as a control, when immunoblotting for cleaved caspase-3. Actin was used as a loading control. Representative blots are from one of two independent experiments. Both biological replicates showed similar results. **g**, Intracellular measurement of NAD⁺ levels in non-cancer cells supplemented with exogenous NAD⁺ (200 μ M) or with the indicated precursors, nicotinic acid (NA), nicotinamide (NM) or nicotinamide riboside (NR) at a concentration of 500 μ M. Data are representative of five biological replicates from five independent experiments (**a–d, g**). Data are mean \pm s.d. *P* values determined by one-way ANOVA with Tukey's multiple comparisons test. For gel source data, see Supplementary Fig. 1.



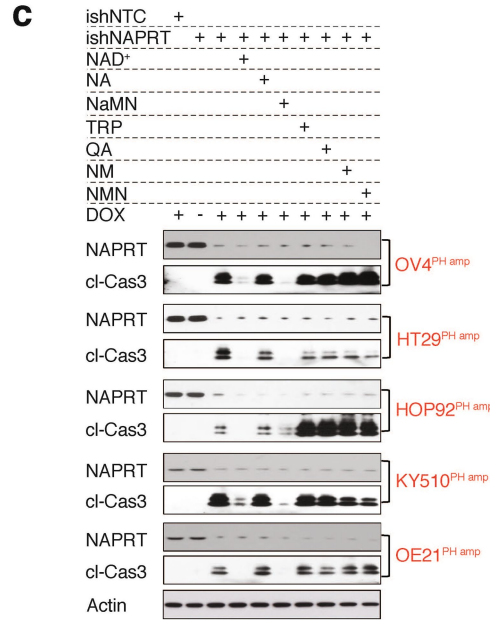
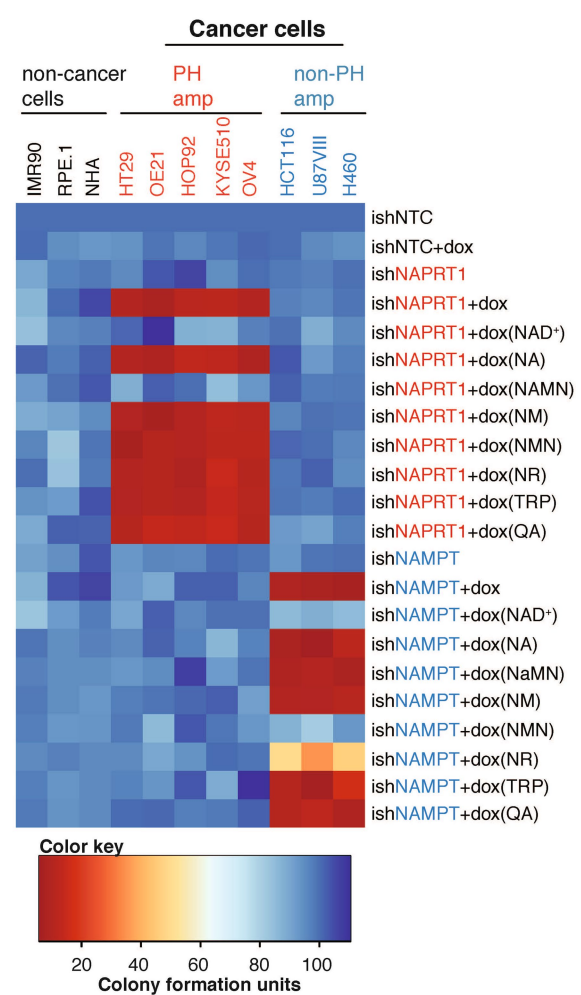
Extended Data Fig. 3 | See next page for caption.

Extended Data Fig. 3 | Tissue context determines the NAD metabolic pathway dependence of cancer cells. **a**, Schematic overview of 54 distinct established cancer models of 13 histological types analysed in the study. H&N, head and neck. **b**, Waterfall plot of cell death as assessed by propidium iodide staining (z score). Both non-cancer and cancer cells ($n = 59$ cell types) were transfected with four different siRNAs targeting *NADSYN1* (red circles), and a non-targeting siNTC (open circle) was used as a negative control. **c**, Heatmap illustrating cell death as measured by propidium iodide staining (z score). Different cancer cell types ($n = 54$ cell lines) were transfected with the indicated siRNAs. **d**, Intracellular

measurement of NAD^+/NADH (left) and NAD^+ (right) levels in non-cancer ($n = 5$ cell types) and cancer ($n = 21$ cell types) cell lines. **e**, Intracellular measurement of NAD^+/NADH (left) and NAD^+ (right) levels in non-cancer cell lines ($n = 5$ cell types) and cancer cell lines amplified (PH-amp) or not amplified (non-PH-amp) for the PH-pathway enzymes NAPRT or NADSYN1 ($n = 21$ cell types). Box and whisker plots are as in Fig. 1d. Data are representative of independent biological replicates from three independent experiments. P values determined by one-way ANOVA with Tukey's multiple comparisons test (**b**) or a two-tailed unpaired Student's t -test (**d, e**).



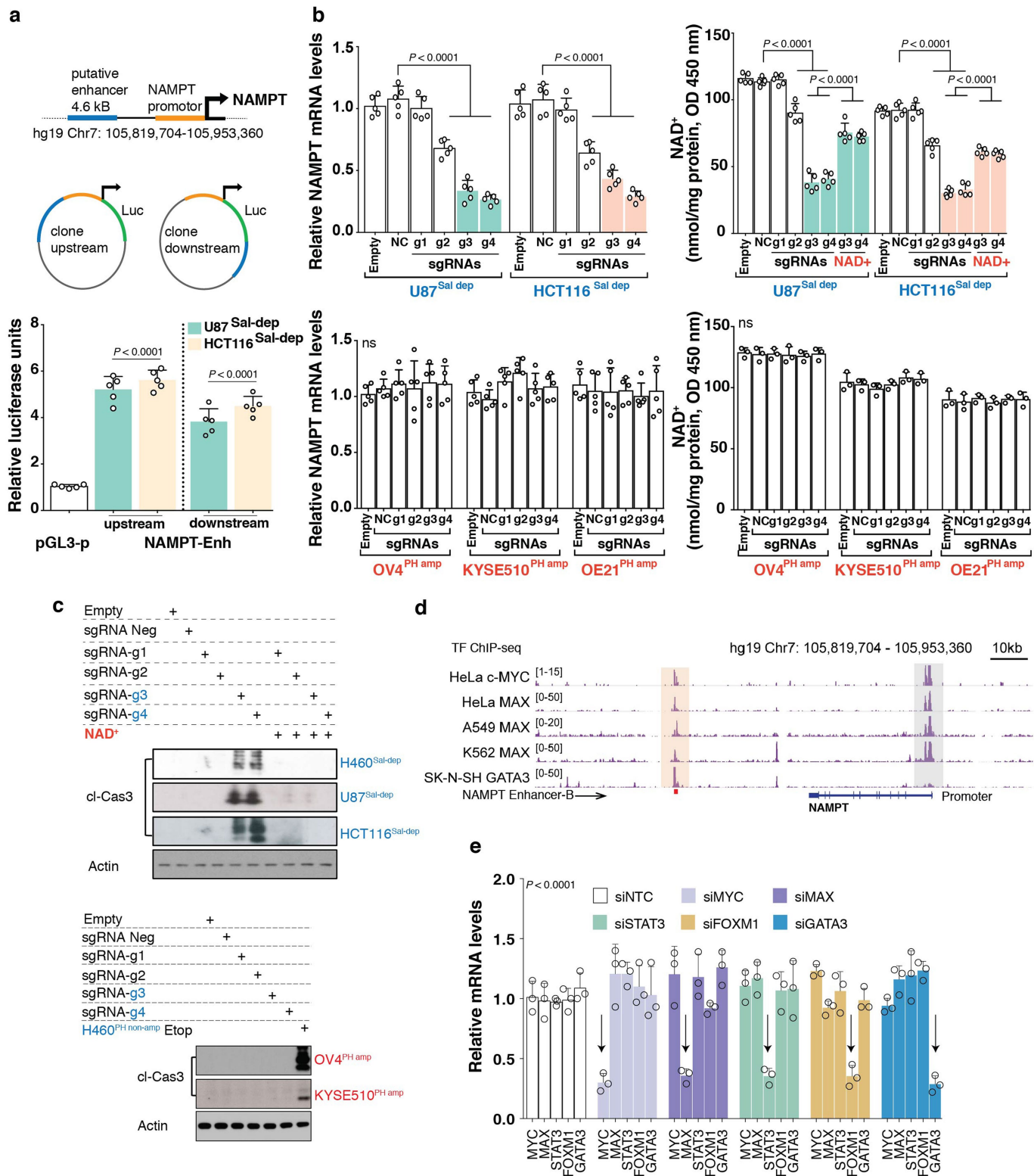
Extended Data Fig. 4 | See next page for caption.



Extended Data Fig. 4 | Genetic depletion of genes encoding key enzymes of NAD biosynthesis pathways combined with metabolic addbacks identify mechanistic basis of NAD pathway addiction.

Cancer cell lines ($n = 8$ cell types) amplified for the PH-pathway enzymes NAPRT or NADSYN1 were transduced independently with the indicated DOX-inducible ishRNAs, followed by DOX treatment after puromycin selection. Non-cancer cell lines (black; $n = 3$ cell types) used as controls were also transduced with the indicated DOX-inducible ishRNAs. Cells were supplemented with fresh growth media and exogenous NAD⁺ (200 μ M) or the indicated precursors, nicotinic acid (NA), nicotinic acid mononucleotide (NAMN), nicotinamide (NM), nicotinamide mononucleotide (NMN), nicotinamide riboside (NR), TRP or quinolinic

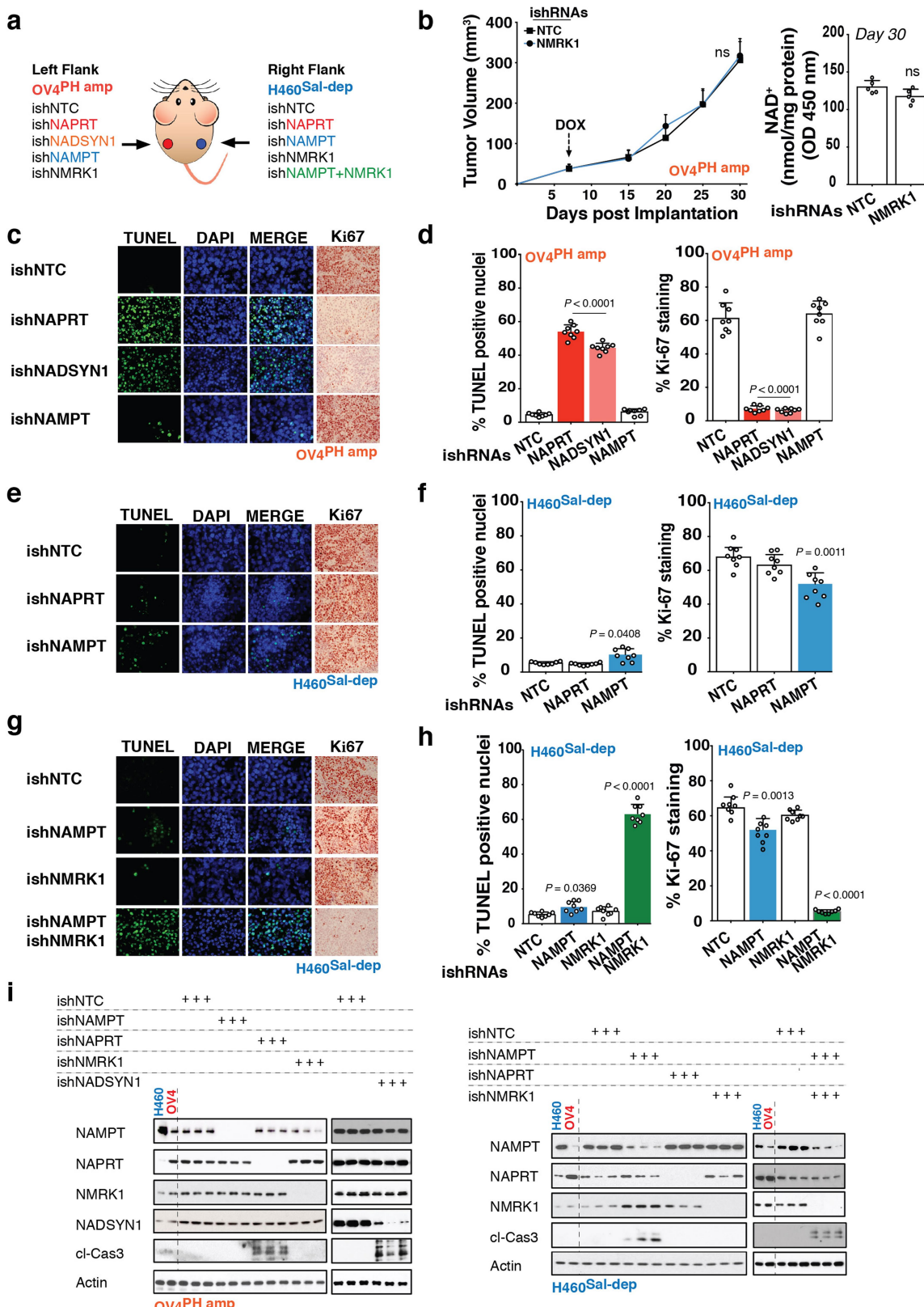
acid (QA) at a concentration of 500 μ M every 2–3 days. **a**, Representative images of colony formation assay using crystal violet staining from one of two independent experiments. Both biological replicates showed similar results. Cells stably expressing different ishRNAs were stained with crystal violet 15–18 days after transduction and selection. **b**, Heatmap illustrating absolute colony formation units. **c**, Immunoblotting for cleaved caspase-3 as a measure of cell death and to test for protein abundance for NAPRT and NAMPT in PH-amplified (left) and non-PH-amplified (right) cancer cells transduced with respective ishRNAs. Actin was used as a loading control. Representative blots from one of two independent experiments. Both biological replicates showed similar results. For gel source data, see Supplementary Fig. 1.



Extended Data Fig. 5 | See next page for caption.

Extended Data Fig. 5 | NAMPT enhancer drives NAD salvage-pathway addiction in cancer. **a**, Luciferase enhancer reporter assay of the putative downstream enhancer. To test the effect of a predicted enhancer, the *cis*-regulatory region of the *NAMPT* locus was cloned into pGL3 reporter constructs in the direction indicated. Enhancer activity of the 4.641-kb *cis*-regulatory region corresponding to the H3K27ac and DHS peak was tested using a luciferase reporter assay, when present both upstream and downstream of the luciferase gene in a construct containing the *NAMPT* promoter. The pGL3 reporter plasmid containing the *NAMPT* promoter but without the enhancer region is used as a negative control (pGL3). Luciferase reporter assay measuring the enhancer activity (NAMPT-Enh) was tested in salvage-dependent, U87^{Sal-dep} and HCT116^{Sal-dep} cancer cells. Relative luciferase units are normalized to *Renilla*. **b**, *NAMPT* transcript levels as measured by qPCR (left), and intracellular measurement of NAD⁺ levels (right) in the indicated cells transduced with the KRAB-dCas9 genetic repression system. **c**, Immunoblotting for abundance of cleaved caspase-3 in cells transduced with the KRAB-dCas9 genetic repression system. Representative blots are from one of two independent experiments. Both biological replicates showed similar results. Actin was used as loading control. When quantifying NAD⁺ and cleaved caspase-3

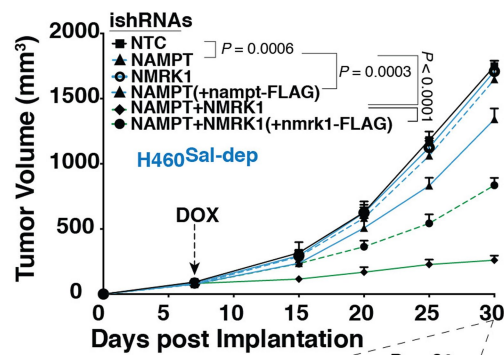
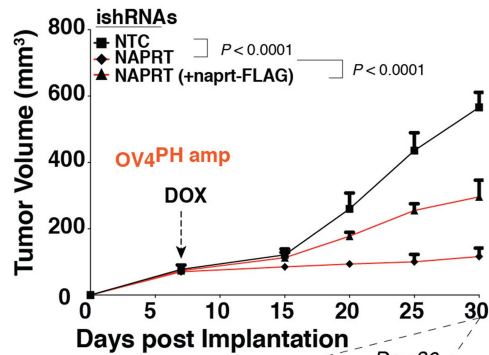
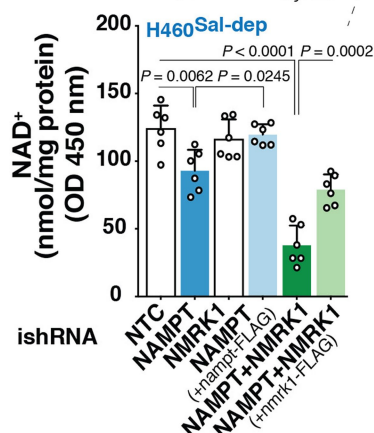
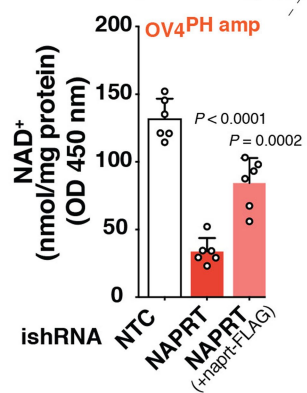
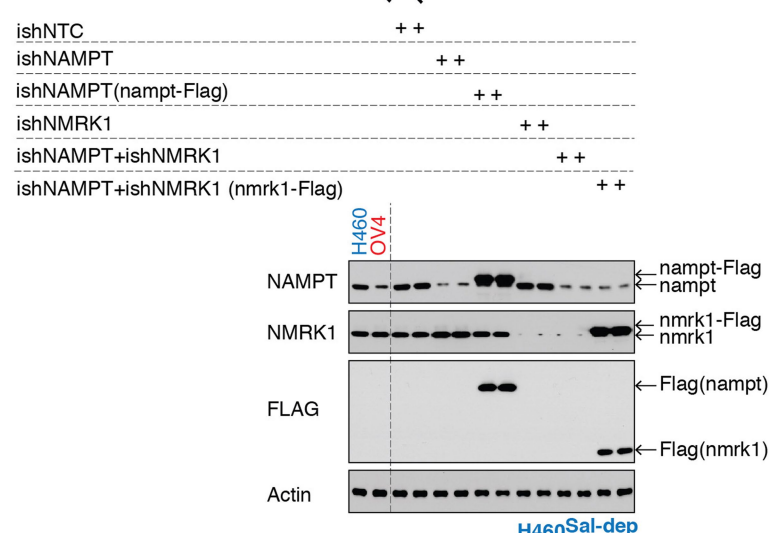
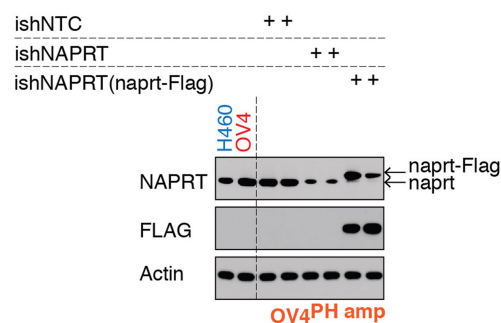
abundance in H460^{Sal-dep}, U87^{Sal-dep} and HCT116^{Sal-dep} cells, exogenous NAD⁺ (200 μM) was added to test for the rescue of the phenotype. See schematic in Fig. 3a for the design of KRAB-dCas9-mediated repression of the *NAMPT* enhancer embedded within the 'B' sub-region. Guide RNAs are as in Fig. 3a. **d**, Genome browser screenshot illustrating transcription factor (TF) ChIP-seq epigenome profiles across several Sal-dep cancer cells (HeLa, A549, K562 and SK-N-SH). The peach shaded region embedding the transcription factor ChIP-seq peaks indicates putative transcription factor recruitment sites that overlap NAMPT 'B' enhancer region (marked by a red square box at the bottom of the clustering, hg19 Chr7: 105,856,541–105,858,299). The grey shaded region corresponds to the *NAMPT* promoter (hg19_dna chr7:105,925,229–105,926,250). **e**, Transcript levels of *MYC*, *MAX*, *STAT3*, *FOXM1* and *GATA3* transcription factor genes in H460^{Sal-dep} cancer cells after siRNA-mediated depletion. Bar plots are representative of five (**a**, **b**) and three (**b**, bottom right, **e**) independent biological replicates from independent experiments. Data are mean ± s.d. *P* values determined by one-way (**a**, **b**) or two-way (**e**) ANOVA with Tukey's multiple comparisons test. For gel source data, see Supplementary Fig. 1.



Extended Data Fig. 6 | See next page for caption.

Extended Data Fig. 6 | In vivo demonstration of NAD metabolic pathway dependencies. **a**, Schematic overview of experiment. OV4^{PH-amp} cells stably expressing DOX-inducible shRNA against *NAPRT*, *NADSYN1*, *NAMPT* or *NMRK1* were inoculated into the left flank of nude mice. H460^{Sal-dep} cells stably expressing DOX-inducible shRNAs were inoculated into the right flank of the same nude mice. ishNTC was used as a non-targeting control for both tumour types. **b**, Tumour volume (left) and intratumoral NAD⁺ measurement (right) of nude mice bearing OV4^{PH-amp} cell stably expressing DOX-inducible shRNA against *NMRK1* taken at the end of experiment on day 30. Tumour volume was monitored over a 30-day period. DOX treatment was initiated on day 7 after implantation until the end of the experiment. **c, e, g**, Representative images illustrating TUNEL⁺ nuclei and Ki67⁺ cells from one of two independent experiments. Both biological replicates showed similar results. **d, f, h**, Quantification of TUNEL⁺ nuclei and Ki67⁺ cells. DAPI was used

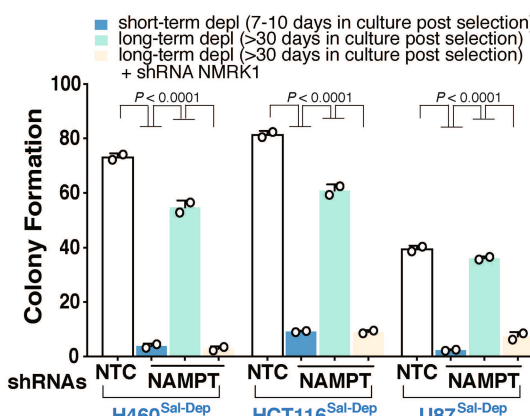
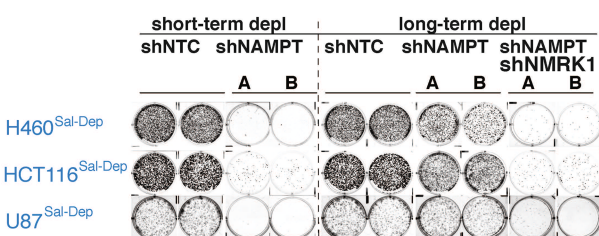
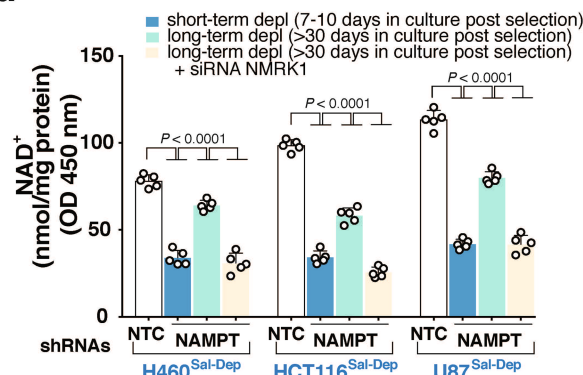
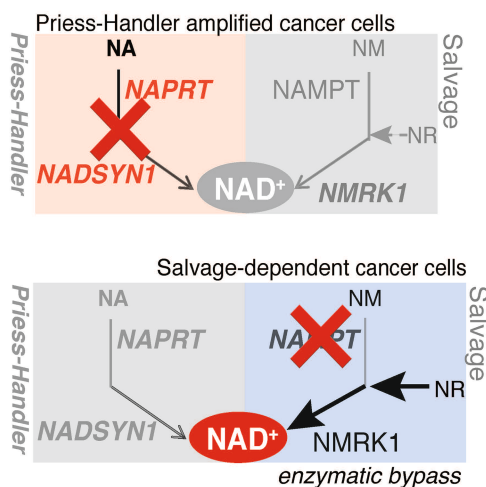
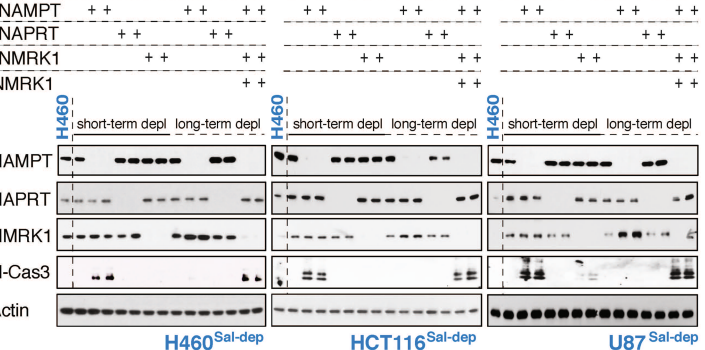
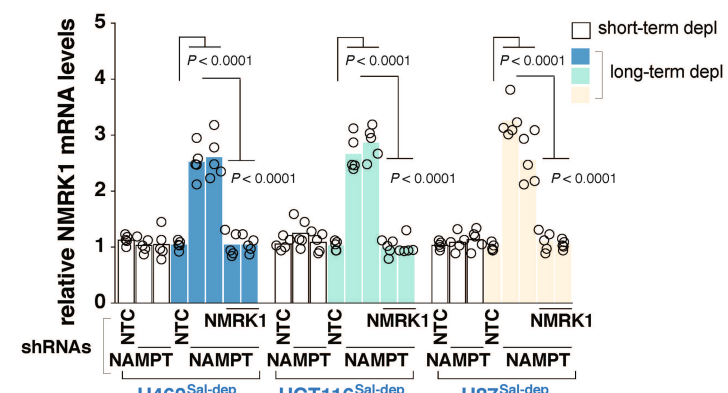
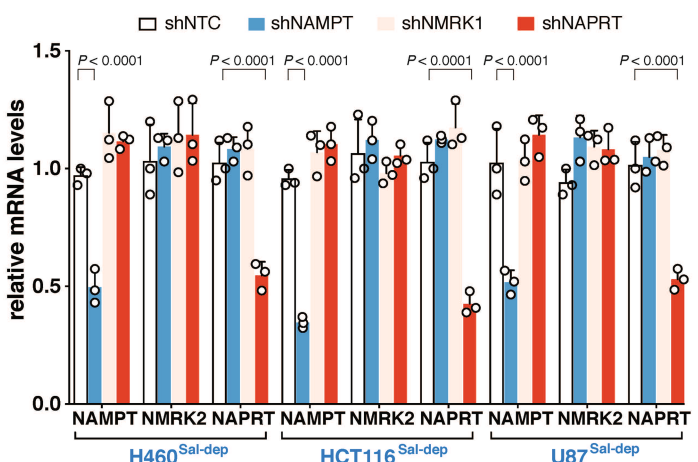
to stain DNA for TUNEL staining. For TUNEL⁺ nuclei, 10,000–12,000 cells were counted for each cohort; for Ki67⁺ cells, 15,000–20,000 cells were counted for each cohort. **i**, Immunoblotting for cleaved-caspase-3 as a measure of cell death and to test for protein abundance of NAMPT, NAPRT, NMRK1 and NADSYN1 in tumour tissues obtained from the indicated tumour types. Representative blots are from one of two independent experiments. Both biological replicates showed similar results. Actin was used as a loading control. Data are representative of eight (**b**, left, **d, f, h**) and five (**b**, right) independent biological replicates from two independent experiments. Data are mean tumour volume \pm s.e.m. ($n = 8$ tumours per cohort), with values determined by two-way ANOVA on repeated measurements over time (**b**, left). Data in scatter plots are mean \pm s.d., with P values determined by one-way ANOVA with Tukey's multiple comparisons test (**d, f, h**). For gel source data, see Supplementary Fig. 1. ns, not significant.

a**b****c****d**

Extended Data Fig. 7 | See next page for caption.

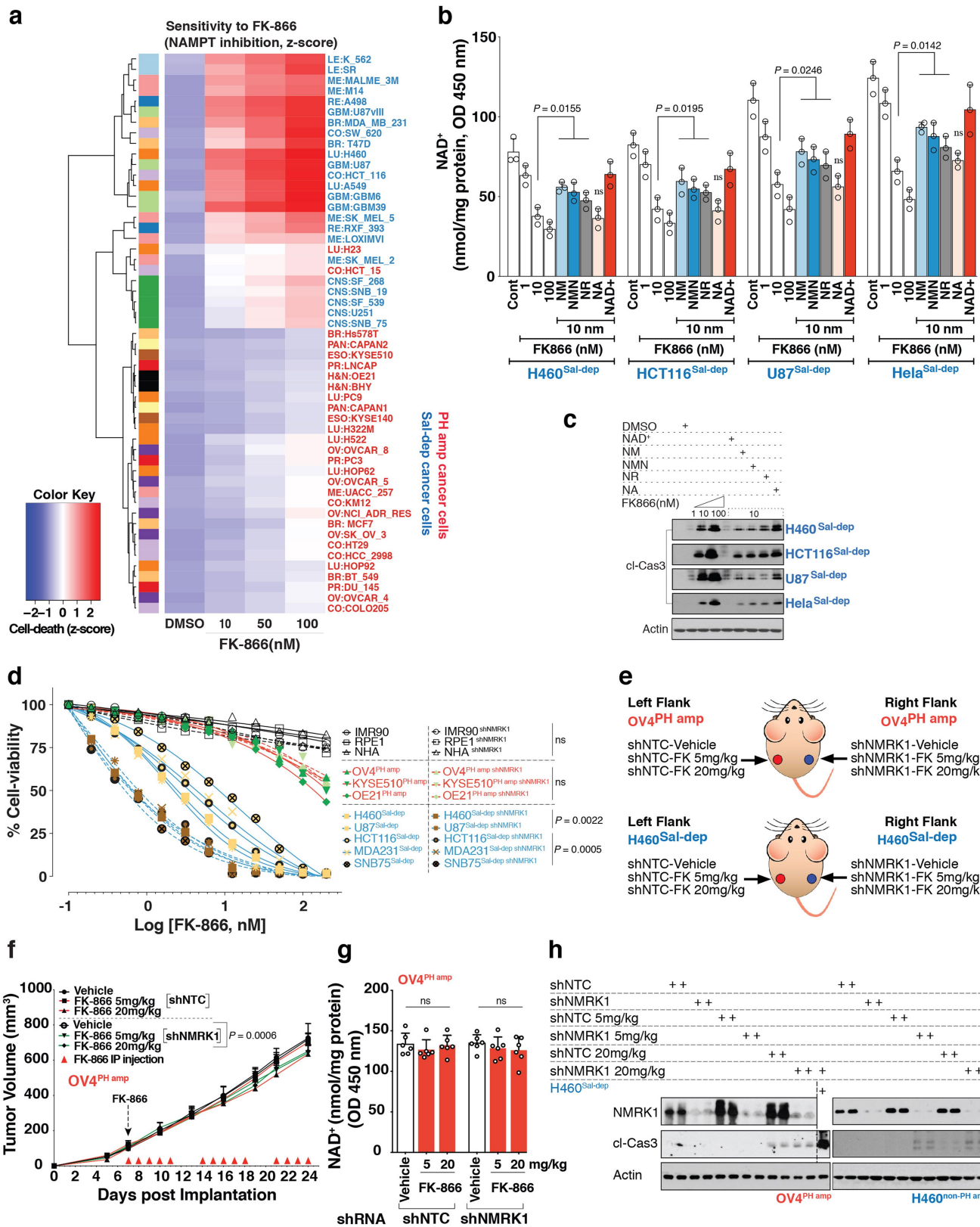
Extended Data Fig. 7 | In vivo genetic depletion of genes encoding key enzymes of NAD biosynthesis pathways combined with genetic rescue identify mechanistic basis of NAD pathway addiction. **a**, Schematic overview of experiment. OV4^{PH-amp} or H460^{Sal-dep} cells stably expressing DOX-inducible shRNA targeting the 3' UTR of the target genes were inoculated into the left flank of individual nude mice as indicated. The same clone of the stably engineered OV4^{PH-amp} or H460^{Sal-dep} cells but with expression of exogenous cDNA corresponding to the target not susceptible to silencing compared to the endogenous copy (ishNAPRT(+naprt-Flag)), (ishNAMPT(+nampt-Flag)) or (ishNAMPT+NMRK1(+nmrk1-Flag)) was inoculated into the right flank of individual mice as indicated. ishNTC was used as a non-targeting control inducible shRNA. **b**, Tumour volume from different tumour types as indicated. Tumour volume was monitored over a 30-day period. DOX treatment was initiated on day

7 after implantation until the end of the experiment. **c**, Intratumoral NAD⁺ measurement of nude mice bearing tumours taken at the end of experiment on day 30 for the indicated tumour types. **d**, Immunoblotting for NAPRT, NAMPT, NMRK1 and Flag in tumour tissues obtained from the indicated tumour types to check for protein abundance. Representative blots are from one of two independent experiments. Both biological replicates showed similar results. Actin was used as a loading control. Data are representative of eight (**b**) or six (**c**) independent biological replicates from two independent experiments. Data are mean tumour volume \pm s.e.m. ($n = 8$ tumours per cohort), with P values determined by two-way ANOVA on repeated measurements over time (**b**). Data in scatter plots are mean \pm s.d., with P values determined by one-way ANOVA with Tukey's multiple comparisons test (**c**). For gel source data, see Supplementary Fig. 1.

a**e****b****c****d**

Extended Data Fig. 8 | NAMPT deficiency leads to enzymatic bypass of the salvage pathway, successfully reprogramming NAD biosynthesis in cancer. Genetically engineered salvage-dependent cancer cells including H460^{Sal-dep}, HCT116^{Sal-dep} and U87^{Sal-dep} were transduced with two different shRNAs against *NAMPT* followed by puromycin selection. A non-targeting shNTC was used a control. **a**, Top, intracellular measurement of NAD⁺ levels. Middle, representative images of clonogenic survival assay using crystal violet staining from one of two independent experiments. Both biological replicates showed similar results. Bottom, quantification of colony formation units. Cells were stained with crystal violet 15–18 days after seeding. Salvage-dependent cancer cells with NAMPT stably silenced grown for an extended duration of time (long-term depletion) were later silenced with shRNA against *NMRK1*. **b**, Immunoblotting for cleaved caspase-3 as a measure of cell death and to test for protein abundance of NAMPT, NMRK1 and NAPRT. Representative blots are from one of two independent experiments. Both biological replicates showed similar results. Actin was used as a loading control. Salvage-dependent cancer cells stably silenced for NAMPT and grown for an extended duration of time (long-term depletion) were later silenced for NMRK1 using siRNA. **c, d**, Relative *NMRK1* and *NAMPT*,

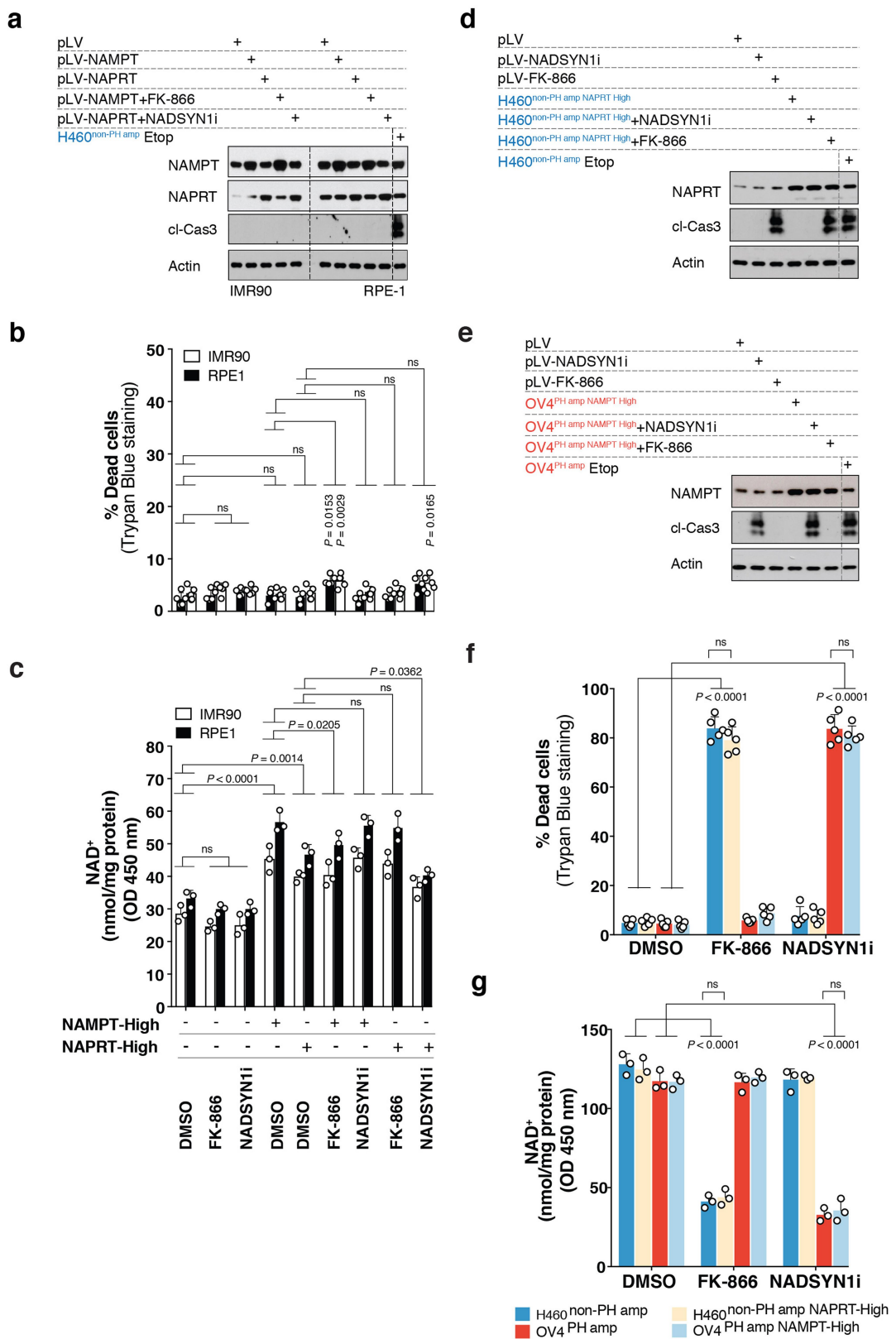
NMRK2 or *NAPRT* transcript levels as measured by qPCR. Salvage-dependent cancer cells stably silenced for NAMPT and grown for an extended duration of time (long-term depletion), were later silenced with *NMRK1* shRNA. **e**, Schematic overview of the model illustrating NAD pathway addiction in cancer is driven by two separate mechanisms—one that gets shaped by gene amplification (left), and the other through epigenetic reprogramming (right). The model demonstrates tissue context-based amplifications of genes encoding key enzymes (NAPRT and NADSYN1) of the PH-pathway and subsequent tumour cell dependence that is absolute and not subjected to enzymatic bypass rewiring. By contrast, epigenetically determined dependence on the NAMPT driven salvage-pathway is subject to enzymatic bypass, requiring combination therapies. In all panels, for short-term depletion, cells were seeded 7–10 days after transduction/selection, and for long-term depletion, cells were seeded \geq 30 days after transduction/selection. Data are representative of five (**a**, top, **c**), three (**d**) and two (**a**, middle, bottom) independent biological replicates from independent experiments. Data in scatter plots are mean \pm s.d., with *P* values determined by one-way ANOVA with Tukey's multiple comparisons test (**a, c, d**). For gel source data, see Supplementary Fig. 1.



Extended Data Fig. 9 | See next page for caption.

Extended Data Fig. 9 | Genetic depletion of *NMRK1* in non-PH-amplified tumour cells enhances sensitivity to FK-866 inducing tumour cell death. **a**, Heatmap illustrating cell death measured by propidium iodide staining (*z* score). Cancer cells were treated with increasing doses of FK-866 for 72 h. **b**, Intracellular measurement of NAD⁺ levels. **c**, Immunoblotting for cleaved caspase-3, in salvage-dependent cancer cells treated with 10 nM FK-866 for 72 h. Cells were supplemented with exogenous NAD⁺ (200 μM) or with the indicated precursors (NM, NMR, NR, NA) at a dose of 500 μM. **d**, Cell viability of non-cancer and cancer cells (PH-amp and sal-dep) stably silenced with shRNA against *NMRK1*, treated with increasing doses of FK-866 for 72 h. **e**, Schematic overview of experiment. OV4^{PH-amp} (top) and H460^{Sal-dep} (bottom) cells stably expressing shRNA against the target gene *NMRK1* were implanted subcutaneously. **f**, Tumour volume of nude mice bearing stably engineered OV4^{PH-amp} cells implanted subcutaneously. Tumour volume was monitored over a 24-day period. Mice were injected intraperitoneally

with FK-866 twice daily. **g**, Intratumoral NAD⁺ measurement of nude mice bearing stably engineered OV4^{PH-amp} tumours, taken at the end of experiment on day 24. **h**, Immunoblotting for cleaved caspase-3 as a measure of cell death and to test for protein abundance for *NMRK1* in tumour tissues obtained from the indicated tumour types. Representative blots are from one of two independent experiments. Both biological replicates showed similar results. Actin was used as a loading control. Data are representative of three (**b**, **d**), eight (**f**) or six (**g**) independent biological replicates from independent experiments. Data in scatter plots (**b**, **g**) are mean ± s.d., with *P* values determined by one-way ANOVA with Tukey's multiple comparisons test. For cell viability data (**d**), *P* values were determined by two-tailed unpaired Student's *t*-test. Data in **f** are mean tumour volume ± s.e.m. (*n* = 8 tumours/cohort), with *P* values determined by two-way ANOVA on repeated measurements over time. For gel source data, see Supplementary Fig. 1.



Extended Data Fig. 10 | See next page for caption.

Extended Data Fig. 10 | Overexpression of rate-limiting NAD biosynthesis enzymes is not sufficient to generate or reverse metabolic addiction. **a**, Immunoblotting for cleaved caspase-3 as a measure of cell-death and to test for abundance of NAMPT and NAPRT protein expression in non-cancer cells (IMR90, RPE-1) stably overexpressing NAMPT or NAPRT. Protein lysates from etoposide-treated H460 cancer cells was used as a control. **b**, Scattered plots represent percentage cell death as assessed by trypan blue exclusion assay. **c**, Intracellular measurement of NAD⁺ levels. **d, e**, Immunoblotting for cleaved caspase-3 as a measure of cell death and to test for abundance of NAPRT (**d**, in H460^{non-PH-amp}) and NAMPT (**e**, in OV4^{PH-amp}) protein expression. Protein lysates from etoposide-treated H460 or OV4 cancer cells was

used as a control. **f**, Scattered plots represent percentage cell death as assessed by trypan blue exclusion assay. **g**, Intracellular measurement of NAD⁺ levels, after stable overexpression of NAPRT or NAMPT in H460 or in OV4 cancer cells as indicated. Stably engineered non-cancer and cancer cells (**a–g**) after selection were treated with FK-866 (10 nM) or NADSYN11i (2 μM) as indicated for 72 h. Representative blots are from one of two independent experiments. Both biological replicates showed similar results. Actin was used as a loading control (**a, d, e**). Data are representative of five (**b, f**) and three (**c, g**) independent biological replicates from independent experiments. Data are mean ± s.d. *P* values determined by two-way ANOVA with Tukey's multiple comparisons test. For gel source data, see Supplementary Fig. 1.

Reporting Summary

Nature Research wishes to improve the reproducibility of the work that we publish. This form provides structure for consistency and transparency in reporting. For further information on Nature Research policies, see [Authors & Referees](#) and the [Editorial Policy Checklist](#).

Statistical parameters

When statistical analyses are reported, confirm that the following items are present in the relevant location (e.g. figure legend, table legend, main text, or Methods section).

n/a Confirmed

- The exact sample size (n) for each experimental group/condition, given as a discrete number and unit of measurement
- An indication of whether measurements were taken from distinct samples or whether the same sample was measured repeatedly
- The statistical test(s) used AND whether they are one- or two-sided
 - Only common tests should be described solely by name; describe more complex techniques in the Methods section.*
- A description of all covariates tested
- A description of any assumptions or corrections, such as tests of normality and adjustment for multiple comparisons
- A full description of the statistics including central tendency (e.g. means) or other basic estimates (e.g. regression coefficient) AND variation (e.g. standard deviation) or associated estimates of uncertainty (e.g. confidence intervals)
- For null hypothesis testing, the test statistic (e.g. F , t , r) with confidence intervals, effect sizes, degrees of freedom and P value noted
 - Give P values as exact values whenever suitable.*
- For Bayesian analysis, information on the choice of priors and Markov chain Monte Carlo settings
- For hierarchical and complex designs, identification of the appropriate level for tests and full reporting of outcomes
- Estimates of effect sizes (e.g. Cohen's d , Pearson's r), indicating how they were calculated
- Clearly defined error bars
 - State explicitly what error bars represent (e.g. SD, SE, CI)*

Our web collection on [statistics for biologists](#) may be useful.

Software and code

Policy information about [availability of computer code](#)

Data collection

Quantitative analysis of the images detecting TUNEL+ nuclei; colonogenic assay using crystal violet for colony formation and protein band intensity was performed using ImageJ software; Quantitative analysis of the IHC images was performed using image analyzing software by Visiopharm; FLOWJO was used to quantify cell-death using flowcytometry;

Data analysis

Graphpad Prism, FLOWJO and ImageJ software

For manuscripts utilizing custom algorithms or software that are central to the research but not yet described in published literature, software must be made available to editors/reviewers upon request. We strongly encourage code deposition in a community repository (e.g. GitHub). See the Nature Research [guidelines for submitting code & software](#) for further information.

Data

Policy information about [availability of data](#)

All manuscripts must include a [data availability statement](#). This statement should provide the following information, where applicable:

- Accession codes, unique identifiers, or web links for publicly available datasets
- A list of figures that have associated raw data
- A description of any restrictions on data availability

DAS statement included. Raw data provided as source data files.

Field-specific reporting

Please select the best fit for your research. If you are not sure, read the appropriate sections before making your selection.

- Life sciences Behavioural & social sciences Ecological, evolutionary & environmental sciences

For a reference copy of the document with all sections, see nature.com/authors/policies/ReportingSummary-flat.pdf

Life sciences study design

All studies must disclose on these points even when the disclosure is negative.

Sample size	No sample-size calculations were performed. Sample size was determined to be adequate based on the magnitude and consistency of measurable differences between groups.
Data exclusions	no data excluded
Replication	The experiments were reliably reproduced by the coauthors listed. Replicated experiments were successful.
Randomization	For xenograft experiments, female athymic nu/nu mice injected with tumor cells were randomized before being allocated to respective cages
Blinding	All other in vitro experiments conducted were not randomized, and investigators were not blinded to either allocation during experiments or to outcome assessments.

Reporting for specific materials, systems and methods

Materials & experimental systems

n/a	Involved in the study
<input checked="" type="checkbox"/>	<input type="checkbox"/> Unique biological materials
<input type="checkbox"/>	<input checked="" type="checkbox"/> Antibodies
<input type="checkbox"/>	<input checked="" type="checkbox"/> Eukaryotic cell lines
<input checked="" type="checkbox"/>	<input type="checkbox"/> Palaeontology
<input type="checkbox"/>	<input checked="" type="checkbox"/> Animals and other organisms
<input checked="" type="checkbox"/>	<input type="checkbox"/> Human research participants

Methods

n/a	Involved in the study
<input type="checkbox"/>	<input checked="" type="checkbox"/> ChIP-seq
<input type="checkbox"/>	<input checked="" type="checkbox"/> Flow cytometry
<input checked="" type="checkbox"/>	<input type="checkbox"/> MRI-based neuroimaging

Antibodies

Antibodies used

The following antibodies were used: PBEF/NAMPT (Cell Signalling Technologies (CST), D1K6D #61122), NAPRT1 (ThermoFischer Scientific, #PA5-31880), NAD Synthetase (Abcam, ab171942), NMRK1 Antibody (Santa cruz, F-8 #sc-398852), NMRK1 (Abcam, Anti-C9orf95 antibody EPR11190 #ab169548), NMRK2 or ITGB1BP3 (ThermoFischer, #PA5-24607). All were used at a dilution of 1:1000. All description about antibodies including manufacturer, species are noted in the method section of the manuscript.

Validation

Validation of each primary antibody for the species and application, were based on manufacturer's statement available on their respective company website

Eukaryotic cell lines

Policy information about [cell lines](#)

Cell line source(s)

The NCI-60 cell-line panel was a gift from A. Shiu (Ludwig Institute of Cancer Research). LNCaP, PC9, CAPAN1, U-87, HEK293, IMR90, HeLa, RPE-1 and MCF10A used in this study were obtained from ATCC. Normal human astrocytes (NHA) were obtained from Lonza. KYSE-510, KYSE-140, BHY were obtained from Leibniz-Institut DSMZ-Deutsche Sammlung von Mikroorganismen und Zellkulturen GmbH, Germany. OE21 was obtained from Sigma. Please refer to Methods.

Authentication

Cell lines were obtained from NCI, ATCC, DSMZ and Sigma and therefore were not authenticated.

Mycoplasma contamination

All cell lines used were tested for mycoplasma contamination. All tested negative.

Commonly misidentified lines
(See [ICLAC](#) register)

Yes--MDA-MB-435, NCI-ADR-RES, and SNB-19. Included as they are part of NCI60.

Animals and other organisms

Policy information about [studies involving animals](#); [ARRIVE guidelines](#) recommended for reporting animal research

Laboratory animals	Five-six-week-old female athymic nu/nu mice were purchased from Harlan Sprague Dawley
Wild animals	Did not involve wild animals
Field-collected samples	Did not involve samples collected from the field.

ChIP-seq

Data deposition

- Confirm that both raw and final processed data have been deposited in a public database such as [GEO](#).
- Confirm that you have deposited or provided access to graph files (e.g. BED files) for the called peaks.

Data access links

May remain private before publication.

For "Initial submission" or "Revised version" documents, provide reviewer access links. For your "Final submission" document, provide a link to the deposited data.

Files in database submission

Provide a list of all files available in the database submission.

Genome browser session (e.g. [UCSC](#))

Provide a link to an anonymized genome browser session for "Initial submission" and "Revised version" documents only, to enable peer review. Write "no longer applicable" for "Final submission" documents.

Methodology

Replicates

Describe the experimental replicates, specifying number, type and replicate agreement.

Sequencing depth

Describe the sequencing depth for each experiment, providing the total number of reads, uniquely mapped reads, length of reads and whether they were paired- or single-end.

Antibodies

Describe the antibodies used for the ChIP-seq experiments; as applicable, provide supplier name, catalog number, clone name, and lot number.

Peak calling parameters

Specify the command line program and parameters used for read mapping and peak calling, including the ChIP, control and index files used.

Data quality

Describe the methods used to ensure data quality in full detail, including how many peaks are at FDR 5% and above 5-fold enrichment.

Software

Describe the software used to collect and analyze the ChIP-seq data. For custom code that has been deposited into a community repository, provide accession details.

Flow Cytometry

Plots

Confirm that:

- The axis labels state the marker and fluorochrome used (e.g. CD4-FITC).
- The axis scales are clearly visible. Include numbers along axes only for bottom left plot of group (a 'group' is an analysis of identical markers).
- All plots are contour plots with outliers or pseudocolor plots.
- A numerical value for number of cells or percentage (with statistics) is provided.

Methodology

Sample preparation

Cell pellets were fixed in 80% EtOH overnight. PBS was added to cell pellets in equal volume to EtOH & stained with Propidium iodide & RNase A. (Check methods sections for details).

Instrument

BD LSRII flow cytometer (BD Biosciences)

Software

FLOWJO

Cell population abundance

Not applicable.

Gating strategy

FSC/SSC gates were marked & that whole population was sub-gated as FSC (area) by FSC (width). 100% of the cells in this gate were used to obtain histograms for PI positivity.

Tick this box to confirm that a figure exemplifying the gating strategy is provided in the Supplementary Information.